Glacial-interglacial changes of $H_2{}^{18}O$, HDO and Deuterium Excess - results from the fully coupled Earth System Model ECHAM5/MPI-OM

M. Werner[1], B. Haese[1, 2], X. Xu[1, 3], X. Zhang[1], M. Butzin[1], G. Lohmann[1]

[1]{Alfred Wegener Institute, Helmholtz Centre for Polar and Marine Sciences, Bremerhaven, Germany}

[2]{Chair for Regional Climate and Hydrology, University of Augsburg, Germany}

[3]{Institute of Geosciences, Department of Geology, Kiel University, Germany}

Correspondence to:

Martin Werner
Alfred Wegener Institute
Helmholtz Centre for Polar and Marine Research
Division Climate Science | Paleoclimate Dynamics
Bussestr. 24
D-27570 Bremerhaven
Germany
email: martin.werner@awi.de

Abstract

In this study we present first results of a new isotope-enabled general circulation model setup. The model consists of a fully coupled atmosphere-ocean model ECHAM5/MPI-OM, enhanced by the interactive land surface scheme JSBACH and an explicit hydrological discharge scheme to close the global water budget. Stable water isotopes $H_2{}^{18}O$ and HDO have been incorporated into all relevant model components. Results of two equilibrium simulations under pre-industrial and last glacial maximum conditions are analysed and compared to observational data and paleoclimate records for evaluating the model's performance of simulating spatial and temporal variations in the isotopic composition of the Earth's water cycle. For the pre-industrial climate, many aspects of the simulation results of meteoric waters are in good to very good agreement with both observations and earlier atmosphere-only simulations. The model is capable of adequately simulating the large spread in the isotopic composition of precipitation between low and high latitudes. A comparison to available ocean data also shows a good model-data agreement, however a strong bias of too depleted ocean surface waters is detected for the Arctic region. Simulation results under last glacial maximum boundary conditions also fit to the wealth of available isotope records from polar ice cores, speleothems, as well as marine calcite data. Data-model evaluation of the isotopic composition in precipitation reveals a good match of the model results and indicates that the temporal glacial-interglacial isotope-temperature relation was substantially lower than the present spatial gradient for most mid- to high-latitudinal regions. As compared to older atmosphere-only simulations, a remarkable improvement is achieved for the modelling of the deuterium excess signal in Antarctic ice cores. Our simulation results indicate that cool sub-tropical and mid-latitudinal sea surface temperatures are key for this progress. A recently discussed revised interpretation of the deuterium excess record of Antarctic ice cores in terms of marine relative humidity changes on glacial-interglacial timescales is not supported by our model results.

1 Introduction

The water cycle is a key component of the Earth's climate system. Documenting and understanding its past evolution is essential to test our ability to model its future changes. Water stable isotopes ($H_2{}^{18}O$, $HD^{16}O$, and $H_2{}^{17}O$) are integrated tracers of climate processes occurring in various branches of this cycle (Craig and Gordon, 1965; Dansgaard, 1964). They have been successfully used to describe past climate changes for more than 30 years. For example, water stable isotopes (hereafter expressed in a δ-notation as $\delta^{18}O$ and δD, with respect to the Vienna Standard Mean Ocean Water standard V-SMOW, if not stated otherwise) have been measured routinely over the past decades in polar ice cores (Jouzel, 2013) and more recently also in non-polar ice cores (Hoffmann et al., 2003; Thompson et al., 1998). To a first order, $\delta^{18}O$ and δD in polar ice cores are used for past temperature reconstructions over the past glacial-interglacial cycles (Jouzel et al., 2007; NEEM community members, 2013). In addition to high-resolution temperature records, the combination of water isotopic ratios permits to have a tracer of the low latitudes in polar ice cores (e.g., Stenni et al., 2010; Vimeux et al., 1999). For other (sub-)tropical isotope archives, e.g. speleothems, some studies have suggested are indicating that the amount of precipitation could be mainly responsible for determining the water isotope concentration (Fleitmann et al., 2003; Wang et al., 2001) – this is called the amount effect (Dansgaard, 1964; Rozanski et al., 1992). Furthermore, in these regions $\delta^{18}O$ and δD might also reflect convective activity along moisture trajectory (Vimeux et al., 2005; Yao et al., 2012), changes to regional moisture sources and the intensity or provenance of atmospheric transport pathways (LeGrande and Schmidt, 2009; Dayem et al., 2010; Lewis et al., 2010; Maher and Thompson, 2012; Caley et al., 2014a; Tan, 2014). High resolution and well-dated records of $\delta^{18}O$ of calcite in tropical speleothems in Asia or South America have therefore been interpreted in terms of past monsoon dynamics (Cruz et al., 2005; Wang et al., 2008). Analogously to continental speleothem archives, the seawater oxygen isotope concentration ($\delta^{18}O_{oce}$) is conserved in carbonates ($\delta^{18}O_c$) from corals, foraminifers, and other marine species. Here, temperature during calcite formation and the isotopic composition of the seawater $\delta^{18}O_c$ are both the key factors controlling $\delta^{18}O_c$ (Shackleton, 1974). Thus, carbonate isotope records from ocean sediment cores are fundamental records to access the water mass changes in a different climate. A considerable body of literature shows that they allow the reconstruction of the three-dimensional structure of the ocean when the number of records is sufficient (Caley et al., 2014b; Roche et al., 2014).

As a second order isotope effect, the deuterium excess – defined as dex = $\delta D - 8 * \delta^{18}O$ – is a quantity, which primarily depends on climatic conditions during evaporative processes (Dansgaard, 1964). According to Merlivat and Jouzel (1979), key parameters that influence the dex signal of the evaporation flux from ocean surface are both relative humidity above the ocean surface as well as water temperature during evaporation. For many years, it has been assumed that relative humidity is remaining almost constant during climate changes and the dex signal of polar ice cores has been used to infer past sea surface temperature changes (Jouzel and Merlivat, 1984; Masson-Delmotte et al., 2005; Steen-Larsen et al., 2014b; Stenni et al., 2001; Vimeux et al., 1999). Recently, Pfahl and Sodemann (2014) have challenged this assumption by arguing that moisture source relative humidity, and not sea surface temperature, is the main driver of dex variability, at least on the present-day seasonal timescale. Their findings are based on the use of an empirical relation between dex and relative humidity together with ERA-Interim reanalysis data (Dee et al., 2011) to globally predict dex values of evaporation fluxes over the ocean. Their results are partly supported by recent monitoring studies of water vapour isotopic composition, which have demonstrated a strong imprint of source humidity in the North Atlantic on the high deuterium excess of Arctic water vapour (Bonne et al., 2014; Steen-Larsen et al., 2014b; 2013).

However, while direct or indirect records of water isotopes in natural archives provide key documentation of past climate variations, their quantitative translation to climate variables such as temperature or precipitation amount still remains uncertain in many cases. Since the beginning, the interpretation of isotopic time series has been almost entirely based on a modern analogue approach. It is assumed that the observed spatial or seasonal relationship between isotopes and surface temperatures, precipitation amount, or salinity provides a calibration, which is also valid for different climates of the past. This hypothesis was originally supported by the close relationship observed between modern annual mean precipitation isotope values and local annual mean temperature, precipitation amounts, or salinity, and for the atmosphere quantitatively it is consistent with a Rayleigh distillation process. However, this hypothesis is increasingly challenged (i) by new present-day observations, (ii) by alternative paleothermometry methods showing changing relationships for past periods (Buizert et al., 2014; Jouzel, 1999). This calls for a revised understanding of the interpretation of water stable isotopes, including second-order parameters such as deuterium excess, and their relationships with climatic conditions influencing the isotope signal.

One key tool for such an improved understanding of water isotopes in the Earth's hydrological cycle are atmospheric and oceanic general circulation models (GCM) with an explicit diagnostics of stable water isotopes. During the last three decades, several such isotope-enabled GCM have been built. Such models provide a mechanistic understanding of the physical processes influencing the isotopic composition of different water bodies in the climate system. They allow the explicit simulation of isotopic fractionation processes during any phase changes of a water mass within the model's hydrological cycle, e.g. during evaporation of water from land or ocean surface, cloud droplet formation, and re-evaporation of droplet water below cloud base. In such a isotope-enabled GCM setup, all relevant factors determining the strength and variability of isotopic fractionation are known.

The early implementations of water stable isotopes in atmospheric models (Hoffmann et al., 1998; Joussaume et al., 1984; Jouzel et al., 1987) have already shown their potential in explaining fundamental physical hydroclimate relationships. Since then, considerable progress has been made in simulating stable water isotopes in climate models, as the climate models have evolved themselves (Risi et al., 2010a; Werner et al., 2011). Using atmospheric models, water stable isotopes have been used for a considerable range of applications at small spatial and temporal scales such as investigating the link between water stable isotopes and decadal variability (Kurita et al., 2011) or to analyse mixing processes within rain events (Lee et al., 2009; Risi et al., 2010b). Many of these atmospheric GCM include at least two stable water isotopes (oxygen-18 and deuterium). With the improvements of the atmospheric GCM in simulating present-day water isotopic content, part of the interest has lately shifted to second order content such as deuterium excess and ^{17}O excess that can provide further constraints on the water cycle but remain challenging (Risi et al., 2010a; Risi et al., 2013; Werner et al., 2011). Besides building atmospheric isotope-enabled GCM, several international groups have also worked on the inclusion of the water isotopes in oceanic GCM. Here, the water isotopic content is a passive tracer once the surface oceanic conditions are determined through the water balance with the atmosphere and the additional fractionation during sea-ice formation and melting. Attempts in oceanic-only GCM have proven useful to challenge the link between oceanic water isotopic content and salinity (Delaygue et al., 2000; Paul et al., 1999; Schmidt, 1998), a subject of considerable interest in paleoceanography.

In general, simulating evolving climate conditions requires using self-contained climate models as much as possible, to avoid prescribing unnecessary or unknown boundary

conditions. In particular for past climates applications, it is necessary to simulated stable water isotopes in the full water cycle system, not only in its atmospheric part. As compared to an atmosphere-only or ocean-only setup, a fully coupled model with an explicit stable water isotope diagnostics will be physically much more consistent regarding relevant fractionation processes during ocean-atmosphere interactions. For past climates, such a coupled isotope model can also generate isotopic compositions in various water reservoirs (e.g. a deuterium excess distribution in ocean surface waters) that are unavailable from proxy data but required as prescribed boundary conditions for uncoupled atmosphere and ocean simulations. So far however, few studies have used fully coupled isotope-enabled climate general circulation models to address questions related to the water cycle. Schmidt et al. (2007) incorporated water isotopes within the water cycle of the Goddard Institute for Space Studies (GISS) coupled ocean-atmosphere model (ModelE). In several multi-centennial simulations, they examined the internal variability and the simulated changes due to orbital and greenhouse gas forcing. Their study was restricted to the modern (preindustrial) and mid-Holocene (6kyrs B.P.) climates. LeGrande et al. (2009) expanded these analyses by performing eight Holocene time slice simulations, each ~1000 years apart. Lewis et al. (2010) used the same GISS-E model for simulating the consequences of a large freshwater input into the North Atlantic as an idealized analogue to iceberg discharge during Heinrich events. As a second fully coupled GCM, the HadCM3 model, has been enhanced by a stable water isotope diagnostics module by Tindall et al. (2009) for analyses of the present-day isotopic signature of El Niño–Southern Oscillation and the tropical amount effect. Besides these two fully coupled isotope-enabled GCM, there have also been some efforts in including water stable isotopes in the hydrological cycle of Earth System Models of Intermediate Complexity (EMICs) by Roche et al. (2004), Brennan et al. (2012), as well as Roche and Caley (2013). These isotope-enabled EMICs can be classified as an alternative tool to test ideas, explore large periods of time in a transient mode and guide much more computationally demanding simulations with fully coupled GCM.

The Paleoclimate Modeling Intercomparison Project (PMIP, http://pmip3.lsce.ipsl.fr) has chosen the Last Glacial Maximum (LGM) climate as one of the target periods for the evaluation of GCM modelling results. The LGM climate is not only very different from the present and/or pre-industrial climate, but this latest glacial epoch offers also a wealth of terrestrial, marine, and ice core proxy data for an in-depth model-data comparison. As many of these data sets are based on water stable isotopes (e.g., speleothem data, marine calcite

data, ice core records) several studies with isotope-enabled GCM have also chosen the LGM as a key period for an evaluation of modelled $\delta^{18}O$ and δD values with different proxy data (Jouzel et al., 2000; Lee et al., 2008; Lewis et al., 2013; Risi et al., 2010a).

Here we present first results of a newly developed isotope-enhanced version of the fully coupled GCM ECHAM5/MPI-OM. The model amalgamates our previous efforts to include stable water isotope diagnostics within the atmosphere GCM ECHAM5 (Werner et al., 2011), the land surface scheme JSBACH (Haese et al., 2013), as well as the ocean GCM MPI-OM (Xu et al., 2012). Our following analysis and presentation of simulation results focus on the following questions: (a) How well does this fully-coupled Earth System Model simulate first-order isotopic variations ($\delta^{18}O$, δD) within different parts of the Earth's water cycle under pre-industrial and LGM boundary conditions? (b) Do the model results indicate substantial changes of the temperature-isotope relation of meteoric water? (c) Are simulated spatial and temporal variations of the deuterium excess in precipitation, a second-order isotope effect, also in agreement with available observations and paleoproxy data? (d) If so, how are these variations of deuterium excess related to past changes of evaporation processes?

2 Model components and simulation setup

2.1 Model components

In this study we use the Earth System Model ECHAM5/MPIOM, formerly also named as Community Earth System Model COSMOS. It is a fully coupled ocean-atmosphere-sea ice-land surface model (Jungclaus et al., 2006), which has now been enhanced by stable water diagnostics in all relevant model components. Previous studies with the standard (non-isotope) version of COSMOS have applied and evaluated this model, among others, for pre-industrial (Wei et al., 2012), glacial and interglacial climate states (Zhang et al., 2014; 2013), the Holocene (Wei and Lohmann, 2012) and Cenozoic climate change (Knorr et al., 2011; Stepanek and Lohmann, 2012).

During the recent years, all key model components (ECHAM5, MPI-OM, JSBACH) have been equipped with a diagnostic module to explicitly simulate both $H_2{}^{18}O$ and HDO within the different parts of the hydrological cycle. Here, we give just a brief summary of key model components and isotope implementation within them and refer to previous publications for details.

The atmosphere component of our model setup is the ECHAM5 atmosphere GCM, which has been mainly built at the Max Planck Institute for Meteorology, Hamburg. The model has a spectral, dynamical core, which is constrained by the equations of state describing the conservation of mass, energy, and momentum. Further model constrains are set by the continuity equation, a prediction equation for the surface pressure, as well as the hydrostatic equation (Roeckner et al., 2003). The water cycle in ECHAM5 contains formulations for evapotranspiration of terrestrial water, evaporation of ocean water, and the formation of large-scale and convective clouds. Within the atmosphere's advection scheme, vapour, liquid and frozen water are transported independently. A detailed model description is given in Roeckner et al. (2003; 2006). Stable water isotopes have been implemented into ECHAM5 in an analogous manner to previous ECHAM model releases (Hoffmann et al., 1998; Werner and Heimann, 2002). The isotope module in ECHAM5 computes the isotopic signal of different water masses within the entire water cycle. Details of the implementation have been reported in Werner at al. (2011). In the atmosphere-ocean coupled setup, ECHAM5 provides the required freshwater flux (P-E) and its isotopic composition for all ocean grid cells to the ocean model MPI-OM.

Within the ECHAM5 model setup used in this study, the JSBACH land surface model calculates the boundary conditions for ECHAM5 over terrestrial areas. This includes the exchange of water, energy, and momentum between the land surface and the atmosphere (Raddatz et al., 2007). JSBACH divides each land surface grid cell into 8 tiles covered by different plant functional types and bare soil. The simulated dynamical vegetation changes are controlled by the processes of natural growing and mortality, as well as disturbance mortality (e.g., wind, fire). Details of this approach are described in Brovkin et al. (2009). The water isotopes $H_2{}^{18}O$ and HDO are almost passive tracers in the JSBACH model. No fractionation of the isotopes is assumed during most physical processes partitioning water masses on the land surface (e.g., snow melt, formation of surface water runoff and drainage; see Haese et al., 2013 for details). For evapotranspiration, fractionation of isotopes might occur during evaporation of water from bare soils. However, the strength of this fractionation remains an open question. In accordance with the results of Haese et al. (2013), we assume in this study that we can ignore any possible fractionation during evapotranspiration processes from terrestrial areas, as our analyses will focus primarily on the isotopic composition of precipitation. This choice might add a small bias to the isotopic composition of terrestrial surface water pools and the discharge of terrestrial net precipitation (P–E) towards the oceans.

Furthermore, it might be relevant for paleoclimate records, where the isotope signal reflects changes in the soil water (e.g., speleothems, ancient groundwater), as a potential fractionation during evapotranspiration processes might lead to substantial changes in the $\delta^{18}O$ and deuterium excess signal of soil water (Haese et al., 2013). However, it remains an open question if such changes would also affect the simulated glacial anomalies ($\Delta_{LGM\text{-}PI}$ $\delta^{18}O$, $\Delta_{LGM\text{-}PI}$ dex), or simply lead to an equivalent strong change of $\delta^{18}O$ and deuterium excess for both the PI and LGM simulations (without any glacial change).

In the used coupled model setup, terrestrial water discharge to the ocean is calculated by the so-called Hydrological Discharge scheme (HD scheme; Hagemann and Gates, 2003). Modelled discharge is calculated with respect to the slope of the topography. For the simulated total river runoff it is assumed that the global water cycle is closed, i.e., all net precipitation (P-E) over terrestrial areas is transported to the ocean. However, lakes are absent in the HD scheme. This may lead to minor errors in the magnitude and location of the modelled river runoff compared to observations. As the ECHAM5/MPI-OM coupled model setup does not include a dynamic ice sheet model, precipitation amounts falling on glaciers are instantaneously put as runoff into to the nearest ocean grid cell for closing the global water budget. Independent of the chosen spatial ECHAM5 model resolution, the HD scheme is always implemented on a fine horizontal 0.5°x0.5° degree grid and allows simulating water mass flows of the major river systems of the Earth. Stable water isotopes $H_2{}^{18}O$ and HDO are incorporated as passive tracers within the HD scheme.

The ocean component of our model setup consists of the general circulation model MPIOM (Marsland et al., 2003), which is employed on a curvilinear Arakawa-C grid. The used MPIOM setup has a free surface and contains subgrid-scale parameterizations for convection, vertical and isopycnal diffusivity, horizontal and vertical viscosity, as well as for the bottom boundary layer flow across steep topography. Sea ice is simulated by a viscous-plastic rheology model (Hibler, 1979). It considers thermodynamic sea ice melt and growth, and also a thermohaline coupling by brine rejection. Stable water isotopes Within MPI-OM, $H_2{}^{18}O$ and HDO are treated as passive tracers. They are fully mixed and advected within the model, and their total mass is conserved. Isotopic variations occur mainly due to temperature-dependent isotope fractionation during evaporation, as well as by advection and mixing of different water masses. Changes of the oceanic water masses by terrestrial freshwater fluxes entering the ocean are included in the model setup, too. For the process of sea ice formation from

liquid waters, the isotopic composition of sea ice is calculated by a liquid to ice equilibrium fractionation factor of 1.003, which is the average from various estimates (Craig and Gordon, 1965; Lehmann and Siegenthaler, 1991; Macdonald et al., 1995; Majoube, 1971). Due to the very low rate of isotopic diffusion in sea ice, we assume no fractionation during sea ice melting. In the atmosphere-ocean coupled setup, MPI-OM provides the isotope composition of sea surface water and sea ice as a temporally varying boundary condition to the atmosphere model ECHAM5.

Within ECHAM5/MPI-OM, atmosphere and ocean are coupled via the Ocean-Atmosphere-Sea Ice-Soil OASIS3 coupler (Valcke et al., 2003). Mass, energy, and momentum fluxes, as well as the related isotope masses of $H_2{}^{18}O$ and HDO, are exchanged between the atmosphere and ocean once per day. The coupling is described in detail in Jungclaus et al. (2006).

2.2 Simulation setup

We have used the following simulation setup for all simulation results presented in this study: The atmospheric component ECHAM5 runs at a horizontal resolution of approx. 3.75°×3.75° with 19 vertical levels between surface and 10hPa (T31L19 resolution). The same horizontal resolution is applied for the land surface scheme JSBACH. The ocean model MPI-OM has a formal horizontal resolution of approx. 3°×1.8° and 40 uneven vertical layers on z-levels. The used MPI-OM model setup has a bipolar orthogonal spherical coordinate system, where the poles are placed over Greenland and Antarctica, respectively. Placing one pole over Greenland avoids a grid singularity in the Arctic Ocean. Furthermore, it ensures a high horizontal grid resolution in the deep-water formation regions of the northern North Atlantic Ocean and the Arctic.

Two different simulations were performed, one for the pre-industrial and one for the LGM climate. We briefly describe here these experimental setups: For the pre-industrial (PI) climate, ECHAM5/MPI-OM has been continued from a PI simulation without isotopes included, which has been in run into equilibrium over several thousand years (Wei et al., 2012; Zhang et al., 2013) using identical PI boundary conditions. At model start, isotope values in the atmosphere have been set to constant values ($\delta^{18}O$: -10‰, δD: -80‰), while the oceanic isotope distribution has been taken from an equilibrium run over 3,000 years with the MPI-OM-wiso ocean model (Xu, 2012) with global mean $\delta^{18}O$ and δD values of 0‰, each (Baertschi, 1976; de Wit et al., 1980). The fully coupled ECHAM5/MPI-OM model with

included isotope diagnostics has then been run under PI boundary conditions (orbital forcing, greenhouse gas concentrations, ocean bathymetry, land surface and ice sheet topography) for another 1,500 years. For the LGM simulation, we impose orbital forcing and greenhouse gas concentrations (CO_2 = 185 ppm; N_2O = 200 ppb; CH_4 = 350 ppb) as well as surface boundary conditions (terrestrial topography, ocean bathymetry, runoff routes according ice sheet reconstruction) in accordance with the PMIP3 protocol (http://pmip3.lsce.ipsl.fr/). An increased global salinity (1 PSU added compared to modern values) accounts for a LGM sea level drop of approx. 116m. Again, the isotope-enabled version of ECHAM5/MPI-OM has been restarted from an already equilibrated simulation without isotopes (Zhang et al., 2013). The initial LGM oceanic $H_2{}^{18}O$ and HDO distribution has been taken from a 3,000yrs long MPI-OM-wiso integration under LGM boundary conditions (Xu, 2012) with a prescribed glacial increase of $\delta^{18}O$ of +1‰. As in previous uncoupled studies (e.g. Risi et al., 2010; Werner et al., 2001) we assume no glacial change of the mean deuterium excess in the ocean, which implies a glacial change of δD of +8‰. The fully coupled ECHAM5/MPI-OM model with included isotope diagnostics has then been run for another 1,500yrs.

At the end of the PI and LGM simulation period, none of the two runs shows any trend in the isotopic composition of ocean surface waters, and $\delta^{18}O$ (δD) trends in deep ocean waters at 2200m are smaller than 0.005‰/100yrs (0.05‰/100yrs). Thus, we rate both simulations as equilibrated and consider the last 100 model years for our analyses.

If not stated otherwise, all reported δ values of meteoric waters (precipitation, evaporation) in this study are calculated as precipitation (or evaporation)-weighted averages with respect to the V-SMOW scale. The δ-values of ocean waters are calculated as arithmetic averages with respect to the V-SMOW scale.

3 Observational data

3.1 GNIP and GISS database

The Global Network of Isotopes in Precipitation (GNIP) was initiated in 1958 by IAEA and WMO, and became operational in 1961 (IAEA/WMO, 2010). Since then, monthly samples of $H_2{}^{18}O$ and HDO in precipitation have been sampled at more than 900 stations from more than 100 different countries. While several stations have continuously collected samples for two or more decades (e.g., GNIP stations in Krakow, Ottawa, Reykjavik, and Vienna), many other

GNIP stations have been in operation for a much shorter period, only. Here, we use a subset of 70 stations from the GNIP database, where surface temperature, precipitation, $\delta^{18}O$, and δD have been reported for a minimum of 5 calendar years, any time within the period 1961 to 2007.

The GISS global seawater oxygen-18 database (Schmidt et al., 1999) is a collection of over 26,000 seawater O-18 values made since about 1950. Partial versions of this database already appeared in Schmidt (1999) and Bigg and Rohling (2000). From this database we are using only values with no applied correction (see Schmidt et al., 1999 for details of the applied corrections). It is important to note that, in contrast to GNIP $\delta^{18}O$ values of precipitation, GISS $\delta^{18}O$ values in ocean water do not represent annual mean values, but are typically measured from a sample taken during an arbitrary day of the year. Therefore, we compare in this study the GISS data not to simulated annual mean isotope values in ocean waters, but to the long-term mean monthly value of the specific month, when a GISS $\delta^{18}O$ value was reported.

3.2 Ice core data

In the late 1960s Dansgaard (1969), Lorius (1979) and others started their pioneering work of analysing polar ice cores for climate research. Since then, the isotopic composition of more than a dozen deep ice cores both from Greenland and Antarctica has been measured. In parallel, alpine ice cores from (sub)tropical regions of South America (Hoffmann et al., 2003; Thompson et al., 1995), Africa (Thompson et al., 2002), and the Tibetan Plateau (Thompson et al., 1989; Tian et al., 2003; Yao et al., 2012) have been drilled an analysed during the last decades, too. In this study we use a subset of 6 Greenland, 10 Antarctic, and 5 (sub)tropical ice cores to compare the measured $\delta^{18}O$ and δD values for the pre-industrial climate and the LGM with our simulation results. For the different ice core records, we take the minimum $\delta^{18}O$ (δD, dex) value of the time interval 19,000 to 23,000 B.P. as a representative mean LGM $\delta^{18}O$ (δD, dex) value. The ice core data used in this study are summarized in Table 1.

3.3 Speleothem calcite data

Recently, Shah et al. (2013) have published a global synthesis of speleothem $\delta^{18}O$ records spanning the period from the LGM until present, which consists of data from 60 speleothems of 36 different sites. From this compilation we have selected a subset of 8 speleothem records

(Table 2), where 1,000yrs-averaged $\delta^{18}O$ values calculated by Shah et al. are available for both the LGM (defined here as period 19,000 to 22,000yrs B.P.) and the most recent 1,000yrs B.P. We use the latter as representative mean PI $\delta^{18}O$ values at the different locations. We are aware that during the last 1,000 years B.P. the climate at a specific speleothem site might have been variable and different from the pre-industrial climate of our ECHAM5/MPI-OM simulation, which could lead to a bias in the model-data comparison. We are also aware that drip water in a cave, which isotopic composition is archived in a speleothem record, might be seasonally biased due to re-evaporation of the precipitated water (Wackerbarth et al., 2010). Furthermore, for many speleothems an additional fractionation between the drip water and the formed calcite can be observed (Dreybrodt and Scholz, 2011). Thus, necessary caution will be taken for the comparison of model results of $\delta^{18}O$ in precipitation with the selected speleothem data.

All listed $\delta^{18}O$ data in Table 2 are measured isotope values in carbonate and refer to the Pee Dee Belemnite (PDB) standard. For comparison with model results, $\delta^{18}O$ values in calcite are converted between the PDB and SMOW scale as the following (Coplen, 1983; Sharp 2007):

$$\delta^{18}O_{c(PDB)} = 0.97002 * \delta^{18}O_{c(SMOW)} - 29.98$$

For an estimation of $\delta^{18}O$ in the drip water we apply a formula linking $\delta^{18}O$ in water and $\delta^{18}O$ in speleothem calcite, derived by Kim and O'Neil (1997) for synthetic calcite:

$$\delta^{18}O_{c(SMOW)} = \delta^{18}O_{water(SMOW)} + 18.03 * (1000/T) - 32.42 + 0.27$$

with T being the temperature (in Kelvin) during calcite formation. As mentioned above, we further assume that the $\delta^{18}O$ values in drip water, calculate in such way, are a reliable proxy for the annual mean $\delta^{18}O$ in precipitation falling at the cave site and can thus be directly compared to our model results.

3.4 Marine calcite data

Caley et al. (2014b) have recently compiled and published a marine calcite $\delta^{18}O$ data set from 114 (115) pairs of deep-sea cores, which contain both LGM and late Holocene planktic (benthic) foraminifera $\delta^{18}O$ data. In their study they report $\delta^{18}O$ anomalies as the change between mean $\delta^{18}O$ values of the period 19,000 to 23,000yrs B.P. and over the last 3,000 years of each record. The MARGO project definition has been used to assure chronostratigraphic quality of the selected data (Kucera et al., 2005). Planktic foraminifera

data have been mainly measured in the following species: *Globigerinoides sacculifer, Globigerinoides ruber pink* and *white*, *Neogloboquadrina pachyderma sinistral*, and *Globigerina bulloides*. Benthic foraminifera data includes, among others, *Cibicidoides wuellerstorfi*, *Cibicidoides pachyderma*, *and Cibicidoides peregrina*. For a more detailed description of this data set we refer to Caley et al. (2014b).

According to Shackleton (1974) the $\delta^{18}O_c$ signal in calcite shells of planktic and benthic foraminifera can be interpreted by the following expression relating temperature to the equilibrium fractionation of inorganic calcite precipitation around 16.9°C:

$$T = 16.9 - 4.38 * (\delta^{18}O_{c(PDB)} - \delta^{18}O_{oce(PDB)}) + 0.1* (\delta^{18}O_{c(PDB)} - \delta^{18}O_{oce(PDB)})^2$$

with T being the temperature during calcite formation, $\delta^{18}O_{c(PDB)}$ the isotopic composition of calcite on the PDB scale, and $\delta^{18}O_{oce(SMOW)}$ the isotopic composition of seawater on the SMOW scale. The conversion between the PDB and SMOW isotope scales (can be expressed as $\delta^{18}O_{oce}$ (PDB) = $\delta^{18}O_{oce}$ (VSMOW) - 0.27 (Hut, 1987).

4 Results and discussion

4.1 Present-day model evaluation

4.1.1 Isotopes in precipitation

Figure 1a shows the global distribution of annual mean $\delta^{18}O$ values in precipitation ($\delta^{18}O_p$) as simulated by the ECHAM5/MPI-OM model with isotope diagnostics included. As for a comparable simulation with the atmosphere-only model ECHAM5-wiso (Werner et al., 2011), all major characteristics of the global $H_2{}^{18}O$ distribution in precipitation as previously reported by Dansgaard (1964) can be found in the global map of $\delta^{18}O_p$. In general, depletion of $\delta^{18}O_p$ is in mid- to high-latitude regions as compared to values in the low latitudes (temperature effect). Strongest depletion of $\delta^{18}O_p$ (down to -54‰) occurs over the polar ice sheets of Antarctica and Greenland. A longitudinal gradient of isotopic depletion in precipitation is simulated from the Atlantic Ocean towards Europe and Eurasia and towards eastern North America (continental effect). Strongly depleted $\delta^{18}O_p$ values are also found over alpine mountain regions like the Andes and the Tibetan Plateau (altitude effect).

For a more quantitative evaluation of the model results, we compare the simulated annual mean $\delta^{18}O_p$ values with observational data from the selected 70 GNIP stations, 21 ice cores,

and 8 speleothems (Chapter 3). To convert the reported speleothem PI values of $\delta^{18}O_c$ in calcite (Table 2) to $\delta^{18}O_p$ in precipitated water, we apply the formulae given in section 3.3. For the required site temperatures, we have interpolated annual mean ERA40 soil temperatures (layer #1, mean of the period 1961-1990) to the different speleothem sites. We find that the modeled $\delta^{18}O_p$ values are in good agreement with the observational data, with a linear correlation coefficient r^2 of 0.97, and a root mean square error (RMSE) of 3.0‰ between measured and modelled $\delta^{18}O_p$ values (Fig. 1b). For an evaluation of the modelled temperature effect (Fig. 1c) we focus on the 71 data sets in mid- to high-latitudinal regions with a annual mean temperature value below 20°C. The modelled global $\delta^{18}O$ -T-gradient (0.58‰/°C; r^2 = 0.96) is close to the observed gradient (0.66‰/°C; r^2 = 0.95), with main deviations caused by an underestimation of depletion for cold regions with mean temperatures below -20°C. This result is similar to the findings for the ECHAM5-wiso atmosphere model, and the deviations can partly be explained by the coarse T31L19 model resolution (Werner et al., 2011). Similar distributions of $\delta^{18}O$ and δD in precipitation have been reported for several atmosphere-only and fully coupled GCM during the last years (e.g., Lee et al., 2007; Risi et al., 2010a; Schmidt et al., 2007; Tindall et al., 2009). While all these models show a reasonable resemblance to GNIP observations for the large-scale patterns in low- and mid-latitudinal regions, some models have difficulties to correctly simulate the very low temperatures and strong isotope depletions over the Antarctic ice sheet (e.g., Lee et al., 2007).

4.1.2 Isotopes in ocean waters

In Fig. 2a, the simulated annual mean $\delta^{18}O_{oce}$ signal in ocean surface waters (mean over the depth interval between surface and 10m) are plotted. Mean values in the tropical to mid-latitudinal oceans range between +0.05‰ to +1.2‰, with a tendency to higher values in the Atlantic Ocean as compared to the Pacific and Indian Ocean. This relative enrichment can be explained by a net freshwater export of Atlantic Ocean water, which is transported westwards to the Pacific (Broecker et al., 1990; Lohmann, 2003; Zaucker and Broecker, 1992). The highest enrichment in the Atlantic Ocean is found south of Bermuda Island with surface water $\delta^{18}O_{oce}$ values of up to +1.3‰. Other, more localized regions of surface water $\delta^{18}O_{oce}$ enrichment with a similar order of magnitude are the Mediterranean Sea, the Black Sea, as well as the Red Sea. Again, this enrichment is most likely caused by a regional surplus of evaporation versus precipitation in these three regions. Stronger than average depletion of $\delta^{18}O_{oce}$ surface waters is simulated for both high-latitudinal ocean regions. While surface

458 waters in the Southern Ocean between 50°S-75°S show a depletion of down to -0.8‰,
459 modelled surface waters in the Arctic Ocean are depleted by down to -1.6‰. This depletion is
460 most likely caused by two effects: (a) the implemented fractionation during sea ice formation
461 which leads to an enrichment (depletion) of the isotopes in sea ice (the remaining liquid
462 water); (b) the inflow of highly depleted water masses of Arctic rivers in combination with a
463 strong stratification of the simulated Arctic Ocean water masses (see below).

464 For a quantitative evaluation of the model results, we compare the simulated values to 3859
465 $\delta^{18}O$ entries of the selected GISS data (Chapter 3.1), which represent surface ocean water
466 values between surface and 10m depth. On a global scale, the simulated $\delta^{18}O_{oce}$ values agree
467 quite well within a range of ±0.25‰ with the GISS values (Fig. 2b). Strongest model-data
468 deviations are found in the following regions: (a) In the vicinity of several large river
469 estuaries the model results reveal too high $\delta^{18}O_{oce}$ values (e.g., at the Amazon and Ganges
470 river mouths); (b) the model also overestimates $\delta^{18}O_{oce}$ in surface water in the Baltic Sea as
471 well as in the Black Sea; (c) for the Arctic Ocean region the comparison yields mixed results:
472 While the MPI-OM model tends to overestimate $\delta^{18}O_{oce}$ in ocean surface waters in some
473 regions by more than +2‰ (e.g. the eastern coast of Greenland, and in the Beaufort Sea north
474 of Alaska), in most other Arctic regions the model results are lower by more than -2‰ than
475 the GISS observations (e.g., in the Hudson Bay area, and the Barents Sea, the Kara Sea, as
476 well as the Laptev Sea).

477 A separation of the model-data comparison into Atlantic, Pacific, Indian, and Arctic Ocean,
478 does not show any systematic deviations between modelled $\delta^{18}O_{oce}$ values and the GISS data
479 for the first three oceans (Fig. 3). We find strong correlations between modelled values and
480 the GISS data as well as a RMSE below 1‰ for all 3 oceans (Atlantic: n = 458, r^2 = 0.91,
481 RMSE = 0.77; Pacific: n = 736, r^2 = 0.60, RMSE = 0.75, Indian Ocean: n = 345, r^2 = 0.46,
482 RMSE = 0.46). The strongest deviations of model values from observational data are caused
483 by the overestimation of $\delta^{18}O_{oce}$ values near river estuaries, at the Baltic Sea, and at the Sea of
484 Okhotsk. For the Arctic Ocean, the majority of the simulated $\delta^{18}O_{oce}$ values is stronger
485 depleted than the corresponding GISS entries and the model-data correlation is worse (n =
486 410, r^2 = 0.33, RMSE = 2.25). This bias in our ECHAM5/MPI-OM model is most likely
487 caused by a too stratified Arctic Ocean. Highly depleted water inflowing from Arctic rivers
488 remains in the upper layers of the Arctic Ocean and is not well mixed with deeper waters.
489 This model deficit is clearly depicted in a comparison of the mean modelled isotope signal

with available measurements from the GISS database in meridional sections of the Atlantic (zonal mean between 60°W-0°W; Fig. 4a, c) and the Pacific basin (zonal mean of region 150°E to 110°W; Fig. 4b, d). For both cross sections, we find that the overestimated depletion of $\delta^{18}O_{oce}$ values in the Artic reaches down to approx. 500m below the surface while simulated North Atlantic Deep Water (NADW) masses are less depleted and in better agreement with the GISS data. Similar low isotope values in the Arctic oceans have already been reported by former studies with ocean-only GCM (Paul et al., 1999; Xu et al., 2012).

In general, we find for the Atlantic Ocean a fair agreement between GISS observations and model values. The regions of the strongest enrichment is located between 40°S to 30°N, with maximum enrichment (+0.6‰ or more) at approx. 20°S and 30°N, and a decreasing trend of enrichment in deeper water until approx. +0.1‰ at a depth of 3,000m. The enriched water masses are also found in NADW below 1,000m, with an enrichment of up to +0.2‰ (Fig. 4a). On the contrary, Atlantic water masses south of 40°S show a relative depletion down to -0.4‰ in their isotopic signature for all water depth, in agreement with available GISS data (Fig. 4c). Depleted water masses stemming from the Antarctic Bottom Water (AABW) are reaching until the equator where the isotopic signal is then mixed with NADW and enriched tropical Atlantic waters. For the Pacific (Fig. 4b) we find a similar vertical and latitudinal $\delta^{18}O_{oce}$ distribution as in the upper layers of the Atlantic Ocean, while the transition zone between enrichment and depletion shoals to approx. 1,000m water depth. Below a depth of approx. 3,500m, depleted AABW ($\delta^{18}O_{oce}$ between -0.4‰ and -0.1‰) fills the entire Pacific. The overall pattern of the Atlantic and Pacific cross sections is in good agreement with a recent study of the *i*LOVECLIM isotope-enabled EMIC (Roche and Caley, 2013) as well as with two ocean-only GCM studies (Paul et al., 1999; Xu et al., 2012).

4.1.3 Discharge of terrestrial surface water

In Fig. 5a, we show the simulated annual mean values of $\delta^{18}O$ for grid cells with a mean inflow of at least $200m^3/s$, as simulated by the HD scheme (see Chapter 2.1), to depict the major river systems on Earth, only. In general, the isotopic composition of a specific river is closely linked to the $\delta^{18}O$ signal of P-E in the catchment area of the particular river. The strongest depletion of down to -12‰ is found for river systems of in high northern regions of Siberia and Alaska, in agreement with observational data (Dodd et al., 2012). For the Rhine, the simulated isotopic composition in the Netherlands is about -7‰ to -8‰, in good agreement with available observations, and similar good agreement is found for the

Mackenzie River in the Canadian Arctic with a modelled outflow signal of -19‰ to -20‰ (Hoffmann et al., 1998). Rivers in mid- and low latitudes contain in general more enriched waters, and the PI model experiment results in least depleted waters (> -4‰) for the Paraná River (Argentina), and the Orange River (South Africa). In the future, the current efforts of the IAEA to build a systematic database of available isotope measurements in rivers (IAEA, 2012) will allow for a more thoroughly evaluation of these model results.

For closing the global water budget, the HD scheme does not only simulate the water transport via large river systems, but also redistributes all net surplus water of terrestrial P-E fluxes to a nearby coastal grid point by following orographic gradients. The $\delta^{18}O$ values of the resulting annual mean water inflow of the coastal grid points to the ocean is shown in Fig. 5b.

4.1.4 Deuterium excess in meteoric and ocean surface waters

In Fig. 6 we show the simulated dex signal in evaporation, precipitation, and ocean surface waters. Dex values in the evaporation flux (Fig. 6a) range between -2‰ and +16‰. The lowest values are found in extreme cold and windy regions of the Arctic, parts of the North Atlantic and above surface waters of the Antarctic Circumpolar Current (ACC). Further negative dex values are simulated for parts of the Sahara and the Arabian Peninsula, but these values occur in regions of extreme low evaporation fluxes from the terrestrial surface and are not meaningful but represent numerical artefacts, caused by the division of two small numerical values for calculating the $\delta^{18}O$ and δD values. Maximum dex values of up to +14‰ are detected in various regions of the Earth, both above terrestrial and marine surfaces. The model results show some agreement to the predicted dex values in evaporation by Pfahl and Sodemann (2014) but it is very difficult to further evaluate this simulated pattern of dex in the evaporation flux, as no systematic data collection of this quantity exists, so far. For precipitation (Fig. 6b), modelled dex_p values range between 0‰ and +18‰ with the highest values in northern parts of the Sahara and a band-like structure covering the mountain regions of Iraq, the Hindu Kush and large parts of the Himalayan plateau. The lowest values occur in dry regions of the southern Sahara and the Arabian Peninsula, northern India, and northern Brazil. The Southern Ocean is another region with simulated low dex_p values. For the Antarctic continent, the large-scale dipole of low (high) dex values in West (East) Antarctica is well captured by the model. For ocean surface waters (Fig. 6d), the simulated variations in deuterium excess are an order of magnitude lower than in precipitation and range between -1.6‰ and +1.6‰. Model results reveal a clear distinction with rather low dex values in mid-

554 to low-latitudinal Atlantic regions, the highest dex values in the Arctic Ocean and the Baltic
555 Sea, and rather small variations (±0.4‰) in the remaining oceans. Both positive and negative
556 anomalies are directly linked to the hydrological balance in the particular regions: In the low-
557 to mid-latitudinal Atlantic Ocean, a net freshwater export exists. As the evaporated and
558 exported water masses have a positive dex composition, the remaining ocean surface waters
559 will become negative in their dex composition due to mass balance. In opposite, a region like
560 the Baltic Sea has a positive mass balance, i.e. total P-E from the Baltic Sea (including its
561 catchment area) is positive and the excess water masses flow via the Skagerrak into the
562 Atlantic Ocean. The surplus of precipitation leads to the positive dex signal in the Baltic Sea.
563 A similar feature is detected for the Arctic Ocean.

564 To evaluate the simulated global distribution of dex in precipitation and ocean surface waters,
565 we use again the GNIP and GISS data sets. The plotted station values in Fig. 6c,e do not show
566 a systematic regional bias of the modelled dex signal in precipitation (Fig. 6c) or ocean
567 surface waters (Fig. 6e). We note that some of the measured dex values, e.g. a series of GISS
568 data points in the Southern Indian Ocean, show strong small-scale variations that cannot be
569 matched due to the coarse horizontal model resolution. However, even on a large-scale
570 average the model results tend to underestimate the dex values in precipitation with a RMSE
571 of 2.9‰ while the simulated dex values of ocean surface waters are in general higher (RMSE:
572 1.8‰) than measurements listed in the GISS database. The modelled slope between the
573 simulated dex in vapour above the ocean surface and the related relative humidity rh
574 (-6.3‰/(10% rh change)) is very close to the value given by Merlivat and Jouzel (1979),
575 though. The combination of underestimation (overestimation) of simulated dex values in
576 precipitation (ocean surface waters) might indicate that the general description of
577 fractionation processes during the evaporation of ocean surface waters, implemented as
578 proposed by Merlivat and Jouzel (1979), should be revised and refined. This finding is in
579 agreement with recent studies by Steen-Larsen et al. (2014b; 2014a; 2015), which reveal
580 substantial deviations of the simulated dex signal in water vapour in Greenland, Bermuda, and
581 Iceland, by several atmosphere GCM as compared to laser-based spectroscopy measurements
582 of isotopes in water vapour.

4.2 Changes of the Last Glacial Maximum

4.2.1 Land surface temperature and precipitation changes

Due to the prescribed changed glacial ice sheet configuration, changed orbital parameters and changed greenhouse gas concentrations the simulated LGM climate on glacier-free terrestrial areas is on average -5.9°C colder than the modeled PI climate. Most regions show a rather uniform cooling in the range of -4°C to -8°C (Fig. 7a). Exceptionally cold regions are mostly adjacent to the prescribed Laurentide and Fennoscandian ice sheet, e.g. part of central North America and central Europe. Another region of exceptional cooling is a large part of Siberia with a cooling of down to -15°C. The only region with a distinct above-average warming is located at Alaska. This region most likely warmed during the LGM due to the increased distance to sea ice-covered Arctic ocean regions, caused by the glacial sea-level drop of approx. 120m. Our results are in overall agreement with the ensemble-mean LGM changes in temperature by the fully coupled climate simulations performed within the PMIP2 and CMIP5/PMIP3 projects (not shown; Braconnot et al., 2007; Harrison et al., 2014). These simulations also indicate for the LGM a maximum cooling of surface temperature over the ice sheets by about -30° and an average cooling of glacier-free land surfaces between -2° and -5°C, except for a colder-than-average Siberian region.

For a comparison with proxy data we compare our model results to the LGM continental temperature and precipitation reconstruction by Bartlein et al. (2011). This reconstruction is mainly based on subfossil pollen and plant macrofossil data. For the 81 sites contained in the temperature dataset of Bartlein et al., the simulated annual mean LGM temperature change is in 24 cases (24 cases) more than 2°C warmer (colder) than the reconstructed temperature change (Fig. 7b). While the model-data deviations of LGM warming anomalies range between +0°C and +20°C, the anomalies of LGM cooling are underestimated by down to -15°C. Several sites with the largest model-data deviations are located near the border of the prescribed Laurentide and Fennoscandinavian ice sheets. These deviations might simply be caused by the rather coarse model resolution of 3.8° x 3.8°, which cannot resolve small-scale temperature changes close to the prescribed glacier area in sufficient detail.

Simulated LGM precipitation changes (Fig. 7c) show a drying of large parts of Siberia and North America, and smaller parts of South America, Africa and East Asia. A wetting is found for the region of California, western Europe, the Brazilian Highlands, South Africa and most parts of Australia. Especially the regions of a wetter LGM climate strongly deviate from older

PMIP2 simulations (Braconnot et al., 2007) but are in good overall agreement with the latest CMIP5 LGM experiments (Harrison et al., 2014). A comparison of the simulation results with the precipitation reconstruction by Bartlein et al. (2011) reveals less agreement between simulated and reconstructed precipitation (Fig. 7c,d). In agreement with the reconstructions, the model simulates a drying over vast parts of Northern Eurasia and Siberia, as well as dipole pattern of wetter (dryer) conditions south of the margin of the Laurentide ice sheet in western (eastern) North America. However, the model fails to simulate a drying of Western and Central Europe during the LGM, as indicated by fossil plant data. Overall, the amplitude of modelled changes in the hydrological cycle (-460mm/year to +270mm/yr) is weaker than the range of the reconstructed changes (-1240mm/yr to +720mm/yr), and the general underestimation of LGM dryness is in line with model results from the PMIP2 and CMIP5/PMIP3 projects (Harrison et al., 2014).

4.2.2 LGM changes of $\delta^{18}O$ in precipitation

Previous studies have already shown that the colder climate of the LGM leads to generally more depleted $\delta^{18}O_p$ values in precipitation (Lee et al., 2008; Risi et al., 2010a). This depletion is a direct consequence of the changed (temperature-dependent) fractionation strength during both evaporation and condensation processes. Over glacier-free land surfaces, we calculate a precipitation-weighted mean decrease of $\delta^{18}O_p$ in precipitation by -0.24‰. For tropical and sub-tropical regions in Mid- and South America, Africa, Australia, and parts of Asia, our simulation reveals almost no LGM-PI changes in $\delta^{18}O_p$ in precipitation (Fig. 8a). Glacial changes of down to -3‰ occur in precipitation over the southern parts of South America and Africa, the Tibetan Plateau, as well as over major parts of Siberia, North America, and Alaska. The strongest simulated LGM-PI changes of $\delta^{18}O_p$ in precipitation (down to -12‰) are found over the glacier areas of both the Northern and Southern Hemisphere. We restrict a first quantitative evaluation of the simulated LGM-PI $\delta^{18}O_p$ anomalies in precipitation to the chosen data of 21 ice cores (Table 1) and 8 speleothem records (Table 2). Our dataset is partly identical to the one used by Risi et al. (2010a) and by Brennan et al. (2012) and enables a direct comparison with these previous model studies. For the ice core records, we compare the modelled change of $\delta^{18}O_p$ in precipitation with the ice core data (Table 1). For the speleothem records, we use both the simulated LGM-PI temperature and $\delta^{18}O_p$ changes to calculate the modelled change of $\delta^{18}O_c$ in calcite, which is then compared with the reconstructions (Table 2). Overall, the model results agree well

(r^2 = 0.64, RMSE = 2.7‰) with the reconstructed LGM-PI $\delta^{18}O$ changes at the various sites (Fig. 8b). The largest deviations are found for the Camp Century ice core (measured LGM-PI $\delta^{18}O_p$ difference: -12.9‰, modelled: -9.5‰) and for the $\delta^{18}O_p$ in precipitation at 4 out of 5 tropical ice core locations.

From the simulated LGM-PI temperature and $\delta^{18}O_p$ changes we calculate the temporal $\delta^{18}O_p$-T-gradient *m* in a specific grid box as $m = (\delta^{18}O_{p,\,LGM} - \delta^{18}O_{p,\,PI}) / (T_{LGM} - T_{PI})$, with T as the surface temperature at the precipitation site. We restrict our calculation to mid- and high-latitude regions with an annual mean PI temperature T_{PI} below +20°C. As a further selection criteria, we use grid cells with a simulated LGM-PI cooling of at least -2°C, only. The calculated temporal $\delta^{18}O_p$-T-gradient *m* for the selected grid cells (N = 1195) ranges between -0.53 and +0.85 (Fig. 8c). For only 18% of the grid cells (N = 218), the calculated temporal $\delta^{18}O_p$-T-gradient ranges between +0.5‰/°C and +0.7‰/°C, close to the simulated modern spatial $\delta^{18}O_p$-T-gradient of *m* = 0.58‰/°C (see Chapter 4.1.1). In a vast majority of the grid cells (79%), the temporal $\delta^{18}O_p$-T-gradient is below the modern spatial one, while a higher temporal gradient is simulated for 3% of the selected cells, only. A clear difference between temporal and spatial $\delta^{18}O_p$-T-gradient has already been reported for Greenland (Buizert et al., 2014; Jouzel, 1999; Werner et al., 2000) and might be caused by different mechanisms (e.g., change in precipitation seasonality, shift of water vapour source regions and transport pathways, varying vertical temperature gradients and atmospheric heights of precipitation formation). However, our results indicate that such a potential bias of the $\delta^{18}O_p$-thermometer (if a modern spatial $\delta^{18}O_p$-T-gradient is used for past temperature reconstructions) might not exist for Greenland, only, but also for large parts of the mid- and high-latitudinal regions. The robustness and implications of these findings will be further investigated in future studies.

Next, we take a more detailed look at the simulation results over both polar ice caps. For the extended compilation of ice core data listed in Table 1, our model results are in good agreement with glacial $\delta^{18}O_p$ anomalies found in Antarctic ice cores (Fig. 9). Mean model-data deviation is 1.1‰ with the largest mismatch for the Byrd ice core (2.5‰). For Greenland, model-data differences are slightly higher than for Antarctica as the model underestimates the LGM-PI $\delta^{18}O_p$ changes by 1.6‰, on average. As already noted above, the largest mismatch is found for the Camp Century ice core (3.4‰). The reason for this stronger model-data mismatch for Greenland as compared to Antarctica could be partly due to the coarse model resolution, or caused by an erroneous warm bias of SST in the source regions of

vapour transported to Greenland. Testing and evaluating these different hypotheses will require further coupled simulations and analyses.

4.2.3 LGM changes of ocean temperatures and marine $\delta^{18}O$ signals

The state of the glacial oceans has been under debate since the first reconstruction of global LGM sea surface temperatures (SST) and sea ice coverage by the CLIMAP group (CLIMAP Project Members, 1976). As compared to CLIMAP, the most recent SST reconstruction by the MARGO project (MARGO Project Members, 2009) indicates, among others, a more pronounced cooling in the eastern mid-latitude North Atlantic than in the western basin, ice-free conditions in the Nordic seas during glacial summer, as well as a 1°C - 3°C cooling of the western Pacific warm pool. The study also revealed the presence of large longitudinal gradients in LGM SST anomalies in all the ocean basins, which are absent in the majority of atmosphere-ocean coupled simulations of the PMIP2 project (MARGO Project Members, 2009).

The physical state of the glacial ocean of our LGM simulation has already been analysed and described in detail by Zhang et al (2013). In agreement with this previous study, we also find a rather uniform SST cooling in the range of 2°C – 4°C during the LGM in our simulation, comparable to the results of several atmosphere-ocean GCM participating in PMIP2 and CMIP5/PMIP3 (Zhuang and Giardino, 2012). For the isotopic composition of ocean surface waters $\delta^{18}O_{oce}$, we simulate a globally averaged mean increase of +0.84‰ as compared to the PI ocean state. This is noteworthy, as we adjusted in our LGM simulation the global ocean isotopic composition by +1‰ to account for the change in global ice volume. A less-than-average part of this increase (0.94‰) is found in surface and shallow water depth down to approx. 1000m, while deeper water masses show a glacial increase of up to +1.06‰ in our simulation. In addition, the simulated glacial increase is not spatially uniform for the ocean surface waters, neither. For most regions the LGM anomalies are in the order of +0.5‰ to +1‰ (Fig. 10a), but more positive LGM $\delta^{18}O_{oce}$ anomalies exist in the ACC region (up to +1.5‰), the Mediterranean region (up to +3‰), as well as in the North Atlantic region above approx. 30°N (up to +2.3‰).

As both water temperatures and $\delta^{18}O_{oce}$ are explicitly simulated by our model setup, we can calculate $\delta^{18}O_{c(PDB)}$ for the PI and LGM simulation and then compare our model results to the marine calcite $\delta^{18}O_c$ dataset documented by Caley et al. (2014b). In agreement with the simulated pattern of LGM $\delta^{18}O_{oce}$ anomalies in seawater, the simulated $\delta^{18}O_c$ changes in

calcite are strongest in the ACC region, the Mediterranean Sea and the North Atlantic. Positive $\delta^{18}O_c$ anomalies reach maximum values of +2.6‰ in the North Atlantic. Comparing the pattern of simulated LGM-PI changes of $\delta^{18}O_{oce}$ in surface waters (Fig. 10a) and $\delta^{18}O_c$ in calcite (Fig. 10b) it is also noteworthy that (a) there exists an additional strong positive LGM $\delta^{18}O_c$ anomaly in the East China Sea and parts of the North Pacific, which has no counterpart in the $\delta^{18}O_{oce}$ changes of ocean surface waters, (b) the $\delta^{18}O_c$ anomalies in the Pacific ACC region are shifted northwards by approx. 5° as compared to the $\delta^{18}O_{oce}$ surface waters anomalies.

A comparison of the simulated $\delta^{18}O_c$ values in ocean surface waters between 0-50m to the $\delta^{18}O_c$ data set of planktic LGM $\delta^{18}O_c$ anomalies compiled by Caley et al. (2014b) shows a systematic overestimation of simulated LGM $\delta^{18}O_c$ changes for the Mediterranean Sea (Fig. 10c). For all three major oceans, our model simulation both underestimates and overestimates LGM $\delta^{18}O_c$ changes at various marine sediment sites. Model-data differences are mostly within the order of the reported uncertainty of the reconstructed LGM $\delta^{18}O_c$ anomalies, as reported by Caley et al. (2014b). The simulated spatial pattern of LGM $\delta^{18}O_c$ anomalies in surface waters shows some remarkable resemblance to the model results of Caley et al. (2014b) using the iLOVECLIM model. In their study, Caley et al. also find the strongest positive $\delta^{18}O_c$ anomalies in the North Atlantic, parts of the northern Pacific as well as in the ACC. In contrast to our simulation, Caley et al. report an additional strong $\delta^{18}O_c$ anomaly in the northern Indian Ocean.

In Fig. 11 mean LGM-PI changes of $\delta^{18}O_c$ for the Atlantic cross section (60°W-0°W) and the Pacific cross section (150°E to 110°W) are shown. For both oceans, model results show the strongest positive change of $\delta^{18}O_c$ between 500m and 3,000m. While $\delta^{18}O_c$ changes of up to +2.6‰ are simulated at around 30°N for the Atlantic basin, the $\delta^{18}O_c$ changes in the Pacific water masses are in general lower (up to +2.2‰) and the region of the largest change is located between 0° and 50°S. The available benthic foraminifera data compiled by Caley et al. (2014b) partly supports these findings. The too positive modelled $\delta^{18}O_c$ values in the North Atlantic in a depth between approx. 2,500m and 4,000m indicate that the simulated NADW formation is probably too strong and too deep. By combining a series of isotope studies with different NADW strengths with available proxy studies of the glacial NADW formation (Duplessy et al., 1980) it should be possible to constrain and improve this aspect of the isotope-enhanced version of the ECHAM5/MPI-OM model. Recently, Roche et al. (2014)

743 presented a similar approach for an improved modelling of Heinrich event 1. However,
744 performing such a set of fully coupled sensitivity experiments is computationally demanding
745 and beyond the scope of this paper.

746 ### 4.2.4 Glacial changes of the deuterium excess

747 In Fig. 12a, we show the global pattern of simulated LGM-PI dex anomalies in precipitation
748 over land surfaces. Changes are rather minor, in the order of -3‰ to +3‰, except for a clear
749 positive anomaly (up to +6‰) in North America south-west of the Laurentide ice sheet
750 margin, and strong negative anomalies (down to -7‰) above Greenland and Antarctica. For
751 ocean surface waters, the simulated dex anomalies are even smaller and almost everywhere in
752 the range of ±1‰ (not shown). Figure 12b shows the simulated LGM-PI dex anomalies in
753 water vapour of the lowest atmospheric model layer above the ocean surface (discussed
754 below).

755 As stated in Chapter 2, we assumed no glacial change of the mean deuterium excess signal in
756 the glacial ocean. However, some recent data (Schrag et al., 2002) suggest a mean glacial dD
757 increase of +7.2‰, which is slightly lower than the increase prescribed in our LGM
758 simulation (+8‰). Such lower glacial dD increase would lead to a mean glacial change of the
759 deuterium excess in ocean waters of -0.8‰. As a first-order estimate, such lowered deuterium
760 excess signal in the ocean might lead to an equivalent lower deuterium excess value both in
761 vapour above the ocean and, consequently, in precipitation, too.

762 So far, ice cores are the only paleoproxy archive, which allow for reconstructing past changes
763 of deuterium excess values in precipitation. In Fig. 13 we compare our model results of
764 annual mean dex changes in precipitation between the LGM and PI simulation with the
765 compiled ice core data (Table 1). Mean absolute deviation between modelled LGM-PI
766 anomalies and ice core data from Antarctica is 1.6‰. For Greenland ice cores, LGM dex
767 values have been only reported for the GRIP ice core, so far. Here, model results
768 underestimate the LGM-PI dex change by 2‰. The overall good agreement between
769 measured and modelled LGM dex changes is remarkable, as isotope-enabled GCM have had
770 some difficulties simulating the measured LGM dex changes in Antarctic ice cores, so far
771 (e.g., Risi et al., 2010a; Werner et al., 2001). As dex values in polar ice cores depend on
772 climate condition during evaporation of the source water, and as the SST of our simulation are
773 more uniform and lower than the latest MARGO reconstruction, one may ask if the good dex
774 agreement is due to the modelled SST. For testing this hypothesis we have conducted an

775 atmosphere-only ECHAM5-wiso simulation with identical LGM boundary conditions as for
776 the fully-coupled ECHAM5/MPI-OM setup but using the GLAMAP LGM SST
777 reconstruction, which was supplemented by older CLIMAP data in order to have global
778 coverage (Schäfer-Neth and Paul, 2003a; 2003b). For $\delta^{18}O_{oce}$ (δD_{oce}), we prescribed a uniform
779 glacial increase of +1‰ (+8‰) in this simulation. In this ECHAM5-wiso sensitivity study,
780 the relatively warm (sub)tropical GLAMAP SST reconstruction leads to smaller simulated
781 negative dex anomalies, or even slightly positive dex anomalies for Vostok and Dome F (Fig.
782 13). The RMSE of all Antarctic ice cores is 2.3‰, which is 0.7‰ worse than in the fully-
783 coupled simulation. We are aware that such a comparison of the fully coupled
784 ECHAM5/MPI-OM setup with an atmosphere-only ECHAM5 experiment with prescribed
785 SST might be hampered by neglecting any atmosphere-ocean feedback in the later.
786 Nevertheless, our simulations indicate that glacial SST, which are cooler than the GLAMAP
787 reconstruction, lead to an improved simulation of dex changes, at least over Antarctica.
788 However, for Greenland the simulated dex anomaly at the GRIP drilling site becomes too low
789 in our fully coupled simulation. But as no more LGM-PI dex records of Greenland ice core
790 records have been published, yet, it remains an open question if this deviation points to a
791 systematic bias in our simulation. More LGM-PI dex data from polar ice cores in combination
792 with further isotope simulations are required to put an additional, highly valuable constraint
793 on available LGM SST reconstructions.

794 Apart from glacial SST changes, changes in the source areas of water transported to
795 Antarctica and Greenland, e.g. by a glacial change in sea ice coverage, might lead to the
796 change in the deuterium excess signal in polar precipitation, too. The simulated sea ice
797 coverage of the COSMOS LGM simulation has already been described in detail in Zhang et
798 al. (2013) and our simulation results are comparable to this previous study. For the southern
799 hemisphere, there is a reasonable agreement between the simulated sea ice concentration and
800 proxy data by Gersonde et al. (2005), such as the austral winter sea ice extent in the Atlantic
801 sector and the austral summer sea ice extent in the Indian ocean sector. However, the
802 simulation might underestimate a larger extent of sporadic summer sea ice between 5°E and
803 5°W in the Southern Ocean, as discussed in Gersonde et al. (2005). As compared to the
804 ECHAM5 experiment with GLAMAP data, a much-reduced sea ice cover in austral summer
805 is found in this coupled ECHAM5/MPI-ESM LGM simulation. This reduction might lead to a
806 stronger contribution of vapour stemming from regions between 60°-65°S to the Antarctic ice
807 sheet. As vapour from these regions has a strong negative deuterium excess signal (cf. Fig.

12) such shift in the source contributions might lead to a more negative deuterium excess signal in Antarctic precipitation, too.

Pfahl and Soedemann (2014) suggest in their study that the typical interpretation of dex variations in ice core records as SST changes might have to be adapted to reflect climatic influences on relative humidity during evaporation. To test this hypothesis, we look at the simulated LGM-PI dex anomalies in water vapour of the lowest atmospheric layer, directly above the ocean surface (Fig. 12b). It is safe to assume that most water transported to Antarctica will stem from Southern Hemisphere marine vapour source regions, and not from continental vapour sources. Simulated LGM-PI dex anomalies of the vapour vary between 0‰ and -5‰ for most ocean regions with a clear gradient towards more negative dex values in the higher latitudinal regions. Plotting these simulated changes of dex in vapour against the modelled relative humidity change between LGM and PI over the ocean surface reveals no correlation between these humidity changes and the simulated dex variations in the vapour layer. As seen in Fig. 14a, simulated LGM values of the relative humidity of the vapour layer above ocean surface varies just by ±5% as compared to the PI values. These rather small variations of the LGM relative humidity changes are somewhat surprising, as cooler SST should lead to cooler air temperatures above the ocean surface, which then should lead to higher relative humidity levels (if the amount of water in the air stays constant). However, we find in our simulations that the air directly above the ocean surface cools slightly stronger during the LGM than the SST themselves. This leads to a reduced glacial evaporation flux from the ocean to the atmosphere, which decreases the relative humidity of the vapour and counterbalance the first effect. Similar small changes of relative humidity changes above the ocean surface and the counterbalance of different effects have recently been reported for a set of CMIP5 climate model results by Laîné et al. (2014). They have analysed a future warmer climate, though. In contrast, modelled LGM SST changes of the Southern Hemisphere cover a range of 0°C to -15°C, and a strong correlation (r^2 = 0.78) between simulated glacial SST changes and LGM dex anomalies in the vapour above the ocean surface is found (Fig. 14b). We rate this finding as a support of the 'classical' interpretation of dex changes in Antarctic ice cores as a proxy for SST changes in the source regions of water transported to Antarctica. However, the correlation between vapour dex and SST changes does not rule out other influencing factors, like wind speed changes, which might affect both the deuterium excess signal and SST changes, simultaneously. Furthermore, we are aware that several recent studies of dex in water vapour have revealed a large bias between measurements and

841 simulations by different isotope-enabled atmospheric GCM (Steen-Larsen et al., 2014b;
842 2015). We cannot resolve this conundrum with the performed simulations and will investigate
843 this topic in more detail in the future.

844 5 Summary and Conclusions

845 In this study we present the first simulations of the fully coupled Earth System Model
846 ECHAM5/MPI-OM. The model has been enhanced by an explicit stable water isotope
847 diagnostics in all relevant model components: atmosphere, land surface, terrestrial discharge,
848 and ocean. The hydrological cycle and its isotopic balance are fully closed in the model setup,
849 and the model has been run successfully into equilibrium under PI and LGM boundary
850 conditions.

851 First-order isotope variations in precipitation ($\delta^{18}O_p$, δD_p) for the PI and LGM climate are in
852 good to very good agreement with available present-day observations from the GNIP
853 database, and with LGM isotope data from various ice core and speleothem records. The
854 largest δ-deviations between present-day observations and model results are found in high-
855 latitudinal regions and are caused by a warm bias of the coupled model, similar to the
856 reported error of the atmosphere-only GCM ECHAM5-wiso (Werner et al., 2011). Such a
857 warm bias, especially over Antarctica, is frequent in GCM (Masson-Delmotte et al., 2006)
858 and is partly related to the coarse spatial resolution of our model setup.

859 The simulated modern spatial δ-T-relation is also in good agreement with the observed one,
860 based on a selection of GNIP and ice core data. A first assessment of the stability of this
861 relation for LGM-PI climate changes reveals that the temporal δ-T-gradient might have been
862 substantially lower than the modern spatial one for most mid- to high-latitudinal regions. Such
863 a deviation, which causes a strong bias in the 'classical' δ-paleothermometry approach, is
864 known for Greenland ice cores (Jouzel, 1999) but has not been discussed for other Northern
865 Hemisphere regions, so far. Future in-depth analyses of our model results can help to achieve
866 an improved interpretation of available isotope records, e.g. from speleothems or permafrost
867 ice wedges (Meyer et al., 2015), from these regions.

868 For the PI climate, simulated marine $\delta^{18}O_{oce}$ values broadly fit to available measurements
869 compiled in the GISS database. For the Atlantic, Pacific, and Indian Ocean the largest model-
870 data deviations in ocean surface waters are found in the vicinity of large river estuaries, the
871 Sea of Okhotsk, parts of the Bering Sea, and the Baltic Sea. Like for the model deficits in

872 $\delta^{18}O_p$, these deviations are most likely related to the rather coarse resolution of the ocean
873 model component MPI-OM, which hampers a realistic simulation of water mass mixing in
874 these coastal regions. For the Arctic, modelled $\delta^{18}O_{oce}$ values in surface waters show a more
875 general negative bias as compared to the GISS data. It remains an open question if this bias
876 can also be simply related to an inadequate mixing of the isotopically depleted inflow of
877 Arctic rivers into this ocean basin, or if a more general model bias in the hydrological balance
878 of the Arctic Ocean exists. For the simulated LGM $\delta^{18}O$ changes, a comparison of model
879 results with available $\delta^{18}O_c$ calcite data from planktic and benthic foraminifera shells reveals a
880 partly model-data match, only. For the North Atlantic, the modelled glacial NADW formation
881 appears too deep and too strong in our LGM simulation. However, more sensitivity studies
882 are necessary to better constrain this aspect of glacial ocean circulation change. As a next
883 step, we will also more explicitly simulate the dependence of $\delta^{18}O_c$ on the surrounding water
884 conditions, and analyse the stability of the relation between $\delta^{18}O$ and salinity in ocean waters
885 under the different climate conditions.

886 The simulation results for second-order changes of $\delta^{18}O$ and δD are also satisfactory. In our
887 analyses, an overall good fit of modern deuterium excess values in precipitation and ocean
888 surface waters with the available observations is found. However, on large-scale average the
889 ECHAM5/MPI-OM isotope results tend to slightly underestimate the dex values in
890 precipitation and, at the same time, overestimate the simulated dex values of ocean surface
891 waters. This combination of opposite biases suggests that the implementation of fractionation
892 processes during the evaporation of ocean surface waters in our model setup, which is strictly
893 following the approach by Merlivat and Jouzel (1979), should maybe be revised and refined
894 in future studies. For LGM-PI changes of deuterium excess, only measurements from
895 Greenland and Antarctic ice cores are available, at present. Our simulation results indicate
896 that LGM Southern Hemisphere SST, which are cooler than the MARGO reconstruction, lead
897 to an improved simulation of dex values in Antarctic precipitation. In addition, our analyses
898 reveal that modelled glacial dex changes are strongly correlation to LGM-PI SST changes, but
899 not to relative humidity changes in the evaporation regions.

900 In this study we have presented first results of the newly developed isotope-enabled version of
901 the Earth System Model ECHAM5/MPI-OM. We have focused on two equilibrium
902 simulations under the pre-industrial and last glacial maximum period, only, due to their
903 different climate states and the wealth of available observational data from both periods.

Future studies will investigate changes in the hydrological cycle and its isotopic composition for further climate periods of the past, e.g. the last interglacial, as well as for the transition between them.

References

Baertschi, P.: Absolute ^{18}O content of standard mean ocean water, Earth Planet. Sci. Lett., 31(3), 341–344, doi: 10.1016/0012-821X(76)90115-1, 1976.

Bartlein, P. J., Harrison, S. P., Brewer, S., Connor, S., Davis, B. A. S., Gajewski, K., Guiot, J., Harrison-Prentice, T. I., Henderson, A., Peyron, O., Prentice, I. C., Scholze, M., Seppä, H., Shuman, B., Sugita, S., Thompson, R. S., Viau, A. E., Williams, J. and Wu, H.: Pollen-based continental climate reconstructions at 6 and 21ka: a global synthesis, Clim. Dyn., 37(3-4), 775–802, doi: 10.1007/s00382-010-0904-1, 2011.

Bigg, G. R. and Rohling, E. J.: An oxygen isotope data set for marine waters, J. Geophys. Res. Oceans, 105(C4), 8527–8535, 2000.

Bonne, J. L., Masson-Delmotte, V., Cattani, O., Delmotte, M., Risi, C., Sodemann, H. and Steen-Larsen, H. C.: The isotopic composition of water vapour and precipitation in Ivittuut, southern Greenland, Atmos. Chem. Phys., 14(9), 4419–4439, doi: 10.5194/acp-14-4419-2014-supplement, 2014.

Braconnot, P., Otto-Bliesner, B., Harrison, S., Joussaume, S., Peterchmitt, J. Y., Abe-Ouchi, A., Crucifix, M., Driesschaert, E., Fichefet, T., Hewitt, C. D., Kageyama, M., Kitoh, A., Laine, A., Loutre, M. F., Marti, O., Merkel, U., Ramstein, G., Valdes, P., Weber, S. L., Yu, Y. and Zhao, Y.: Results of PMIP2 coupled simulations of the Mid-Holocene and Last Glacial Maximum - Part 1: experiments and large-scale features, Clim Past, 3(2), 261–277, 2007.

Brennan, C. E., Weaver, A. J., Eby, M. and Meissner, K. J.: Modelling oxygen isotopes in the University of Victoria Earth System Climate Model for pre-industrial and last glacial maximum conditions, Atmosphere-Ocean, 50(4), 447–465, doi: 10.1080/07055900.2012.707611, 2012.

Broecker, W. S., Peng, T. H., Jouzel, J. and Russell, G.: The magnitude of global fresh-water transports of importance to ocean circulation, Clim. Dyn., 4(2), 73–79, doi: 10.1007/BF00208902, 1990.

Brovkin, V., Raddatz, T., Reick, C. H., Claussen, M. and Gayler, V.: Global biogeophysical interactions between forest and climate, Geophys. Res. Lett., 36, doi: 10.1029/2009gl037543, 2009.

Buizert, C., Gkinis, V., Severinghaus, J. P., He, F., Lecavalier, B. S., Kindler, P., Leuenberger, M., Carlson, A. E., Vinther, B., Masson-Delmotte, V., White, J. W. C., Liu, Z., Otto-Bliesner, B. and Brook, E. J.: Greenland temperature response to climate forcing during the last deglaciation, Science, 345(6201), 1177–1180, 2014.

Caley, T., Roche, D. M. and Renssen, H.: Orbital Asian summer monsoon dynamics revealed using an isotope- enabled global climate model, Nature Communications, 5, doi:10.1038/ncomms6371, 2014a.

Caley, T., Roche, D. M., Waelbroeck, C. and Michel, E.: Oxygen stable isotopes during the Last Glacial Maximum climate: perspectives from data–model (iLOVECLIM) comparison, Clim Past, 10(6), 1939–1955, doi: 10.5194/cp-10-1939-2014, 2014b.

CLIMAP Project Members: Surface of Ice-Age Earth, Science, 191(4232), 1131–1137, 1976.

Coplen, T. B., Kendall, C., and Hopple, J.: Comparison of stable isotope reference samples, Nature, 302, 236–238, 1983.

Craig, H. and Gordon, L. I.: Deuterium and oxygen 18 variations in the ocean and the marine atmosphere, edited by E. Tongiogi, pp. 9–130, Consiglio nazionale delle richerche, Laboratorio de geologia nucleare, Spoleto, Italy. 1965.

955 Cruz, F. W., Burns, S. J., Karmann, I., Sharp, W. D., Vuille, M., Cardoso, A. O., Ferrari, J.
956 A., Dias, P. L. S. and Viana, O.: Insolation-driven changes in atmospheric circulation over
957 the past 116,000 years in subtropical Brazil, Nature, 434(7029), 63–66, doi:
958 10.1038/Nature03365, 2005.
959 Dansgaard, W.: Stable isotopes in precipitation, Tellus, 16(4), 436–468, 1964.
960 Dansgaard, W., Johnsen, S. J., Møller, J. and Langway, C. C.: Oxygen isotope record for the
961 Camp Century Greenland ice core, Science, 166, 377, 1969.
962 Dayem, K. E., Molnar, P., Battisti, D. S. and Roe, G. H.: Lessons learned from oxygen
963 isotopes in modern precipitation applied to interpretation of speleothem records of
964 paleoclimate from eastern Asia, Earth Planet. Sci. Lett., 295(1-2), 219–230,
965 doi:10.1016/j.epsl.2010.04.003, 2010.
966 de Wit, J. C., van der Straaten, C. M. and Mook, W. G.: Determination of the absolute
967 hydrogen isotopic ratio of V-SMOW and SLAP, Geostandards Newsletter, 4(1), 33–36,
968 doi: 10.1111/j.1751-908X.1980.tb00270.x, 1980.
969 Dee, D. P., Uppala, S. M., Simmons, A. J., Berrisford, P., Poli, P., Kobayashi, S., Andrae, U.,
970 Balmaseda, M. A., Balsamo, G., Bauer, P., Bechtold, P., Beljaars, A. C. M., van de Berg,
971 L., Bidlot, J., Bormann, N., Delsol, C., Dragani, R., Fuentes, M., Geer, A. J., Haimberger,
972 L., Healy, S. B., Hersbach, H., Holm, E. V., Isaksen, L., Kallberg, P., Kohler, M.,
973 Matricardi, M., McNally, A. P., Monge-Sanz, B. M., Morcrette, J. J., Park, B. K., Peubey,
974 C., de Rosnay, P., Tavolato, C., Thepaut, J. N. and Vitart, F.: The ERA-Interim reanalysis:
975 configuration and performance of the data assimilation system, Q. J. Roy. Meteor. Soc.,
976 137(656), 553–597, doi: 10.1002/Qj.828, 2011.
977 Delaygue, G., Jouzel, J. and Dutay, J. C.: Oxygen 18-salinity relationship simulated by an
978 oceanic general circulation model, Earth Planet. Sci. Lett., 178(1-2), 113–123, doi:
979 10.1016/S0012-821X(00)00073-X, 2000.
980 Dodd, P. A., Rabe, B., Hansen, E., Falck, E., Mackensen, A., Rohling, E., Stedmon, C. and
981 Kristiansen, S.: The freshwater composition of the Fram Strait outflow derived from a
982 decade of tracer measurements, J. Geophys. Res., 117(C11), C11005, 2012.
983 Dreybrodt, W. and Scholz, D.: Climatic dependence of stable carbon and oxygen isotope
984 signals recorded in speleothems: From soil water to speleothem calcite, Geochim.
985 Cosmochim. Acta, 75(3), 734–752, doi: 10.1016/j.gca.2010.11.002, 2011.
986 Duplessy, J. C., Moyes, J. and Pujol, C.: Deep-water formation in the North-Atlantic Ocean
987 during the last Ice-Age, Nature, 286(5772), 479–482, 1980.
988 Fleitmann, D., Burns, S. J., Mudelsee, M., Neff, U., Kramers, J., Mangini, A. and Matter, A.:
989 Holocene Forcing of the Indian Monsoon Recorded in a Stalagmite from Southern Oman,
990 Science, 300(5626), 1737–1739, doi: 10.1126/science.1083130, 2003.
991 Gersonde, R., Crosta, X., Abelmann, A. and Armand, L.: Sea-surface temperature and sea ice
992 distribution of the Southern Ocean at the EPILOG Last Glacial Maximum - A circum-
993 Antarctic view based on siliceous microfossil records, Quaternary Sci Rev, 24(7-9), 869–
994 896, doi:10.1016/j.quascirev.2004.07.015, 2005.
995 Haese, B., Werner, M. and Lohmann, G.: Stable water isotopes in the coupled atmosphere–
996 land surface model ECHAM5-JSBACH, Geosci. Model Dev., 6(5), 1463–1480, doi:
997 10.5194/gmd-6-1463-2013, 2013.
998 Hagemann, S. and Gates, L. D.: Improving a subgrid runoff parameterization scheme for
999 climate models by the use of high resolution data derived from satellite observations, Clim.
1000 Dyn., 21(3-4), 349–359, doi: 10.1007/s00382-003-0349-x, 2003.

1001 Harrison, S. P., Bartlein, P. J., Brewer, S., Prentice, I. C., Boyd, M., Hessler, I., Holmgren, K.,
1002 Izumi, K. and Willis, K.: Climate model benchmarking with glacial and mid-Holocene
1003 climates, Clim. Dyn., 43(3-4), 671–688, doi: 10.1007/s00382-013-1922-6, 2014.
1004 Hibler, W. D.: A dynamic thermodynamic sea ice model, J. Phys. Oceanogr., 9(4), 815–846,
1005 1979.
1006 Hoffmann, G., Werner, M. and Heimann, M.: Water isotope module of the ECHAM
1007 atmospheric general circulation model: A study on timescales from days to several years, J.
1008 Geophys. Res. Atmos., 103(D14), 16871–16896, 1998.
1009 Hoffmann, G., Ramirez, E., Taupin, J. D., Francou, B., Ribstein, P., Delmas, R., Durr, H.,
1010 Gallaire, R., Simoes, J., Schotterer, U., Stiévenard, M. and Werner, M.: Coherent isotope
1011 history of Andean ice cores over the last century, Geophys. Res. Lett., 30(4), doi:
1012 10.1029/2002gl014870, 2003.
1013 Hut, G.: Stable Isotope Reference Samples for Geochemical and Hydrological Investigations.
1014 Consultant Group Meeting IAEA, Vienna 16–18 September 1985, Report to the Director
1015 General, International Atomic Energy Agency, Vienna, 1987.
1016 IAEA: Global Network of Isotopes in Rivers, available from: http://www-
1017 naweb.iaea.org/napc/ih/IHS_resources_gnir.html, 2012.
1018 IAEA/WMO: Global Network of Isotopes in Precipitation: The GNIP Database, available
1019 from: http://www.iaea.org/water, 2010.
1020 Johnsen, S. J., Dansgaard, W., Clausen, H. B. and Langway, C. C.: Oxygen isotope profiles
1021 through the Antarctic and Greenland ice sheets, Nature, 235(5339), 429–434, 1972.
1022 Johnsen, S. J., Dahl-Jensen, D., Gundestrup, N., Steffensen, J. P., Clausen, H. B., Miller, H.,
1023 Masson-Delmotte, V., Sveinbjornsdottir, A. E. and White, J.: Oxygen isotope and
1024 palaeotemperature records from six Greenland ice-core stations: Camp Century, Dye-3,
1025 GRIP, GISP2, Renland and NorthGRIP, J. Quat. Sci., 16(4), 299–307, 2001.
1026 Joussaume, S., Sadourny, R. and Jouzel, J.: A general circulation model of water isotope
1027 cycles in the atmosphere, Nature, 311(5981), 24–29, 1984.
1028 Jouzel, J.: Calibrating the isotopic paleothermometer, Science, 286(5441), 910–911, 1999.
1029 Jouzel, J.: A brief history of ice core science over the last 50 yr, CP, 9(6), 2525–2547, doi:
1030 10.5194/cp-9-2525-2013, 2013.
1031 Jouzel, J. and Merlivat, L.: Deuterium and oxygen 18 in precipitation: modeling of the
1032 isotopic effects during snow formation, J. Geophys. Res., 89(D7), 11749–11575, 1984.
1033 Jouzel, J., Russell, G. L., Suozzo, R. J., Koster, R. D., White, J. W. C. and Broecker, W. S.:
1034 Simulations of the HDO and $H_2{}^{18}O$ atmospheric cycles using the NASA GISS general
1035 circulation model: the seasonal cycle for present-day conditions, J. Geophys. Res.,
1036 92(D12), 14739–14760, 1987.
1037 Jouzel, J., Hoffmann, G., Koster, R. D. and Masson, V.: Water isotopes in precipitation:
1038 data/model comparison for present-day and past climates, Quaternary Sci Rev, 19(1-5),
1039 363–379, 2000.
1040 Jouzel, J., Masson-Delmotte, V., Cattani, O., Dreyfus, G., Falourd, S., Hoffmann, G., Minster,
1041 B., Nouet, J., Barnola, J. M., Chappellaz, J., Fischer, H., Gallet, J. C., Johnsen, S.,
1042 Leuenberger, M., Loulergue, L., Luethi, D., Oerter, H., Parrenin, F., Raisbeck, G.,
1043 Raynaud, D., Schilt, A., Schwander, J., Selmo, E., Souchez, R., Spahni, R., Stauffer, B.,
1044 Steffensen, J. P., Stenni, B., Stocker, T. F., Tison, J. L., Werner, M. and Wolff, E. W.:
1045 Orbital and millennial Antarctic climate variability over the past 800,000 years, Science,
1046 317(5839), 793–796, doi: 10.1126/science.1141038, 2007.

1047 Jungclaus, J. H., Keenlyside, N., Botzet, M., Haak, H., Luo, J. J., Latif, M., Marotzke, J.,
1048 Mikolajewicz, U. and Roeckner, E.: Ocean circulation and tropical variability in the
1049 coupled model ECHAM5/MPI-OM, J. Climate, 19(16), 3952–3972, 2006.
1050 Kim, S. T. and ONeil, J. R.: Equilibrium and nonequilibrium oxygen isotope effects in
1051 synthetic carbonates, Geochim. Cosmochim. Acta, 61(16), 3461–3475, 1997.
1052 Knorr, G., Butzin, M., Micheels, A. and Lohmann, G.: A warm Miocene climate at low
1053 atmospheric CO 2levels, Geophys. Res. Lett., 38(20), doi: 10.1029/2011GL048873, 2011.
1054 Kucera, M., Rosell-Mele, A., Schneider, R., Waelbroeck, C. and Weinelt, M.: Multiproxy
1055 approach for the reconstruction of the glacial ocean surface (MARGO), Quaternary Sci
1056 Rev, 24(7-9), 813–819, doi: 10.1016/j.quascirev.2004.07.017, 2005.
1057 Kurita, N., Noone, D., Risi, C., Schmidt, G. A., Yamada, H. and Yoneyama, K.: Intraseasonal
1058 isotopic variation associated with the Madden-Julian Oscillation, J. Geophys. Res. Atmos.,
1059 116, doi: 10.1029/2010JD015209, 2011.
1060 Laîné, A., Nakamura, H., Nishii, K. and Miyasaka, T.: A diagnostic study of future
1061 evaporation changes projected in CMIP5 climate models, Clim. Dyn., 42(9-10), 2745–
1062 2761, doi:10.1007/s00382-014-2087-7, 2014.
1063 Lee, J.-E., Fung, I., DePaolo, D. J. and Henning, C. C.: Analysis of the global distribution of
1064 water isotopes using the NCAR atmospheric general circulation model, J. Geophys. Res.
1065 Atmos., 112(D16), doi: 10.1029/2006JD007657, 2007.
1066 Lee, J.-E., Fung, I., DePaolo, D. J. and Otto-Bliesner, B.: Water isotopes during the Last
1067 Glacial Maximum: New general circulation model calculations, J. Geophys. Res.,
1068 113(D19), D19109, doi: 10.1029/2008JD009859, 2008.
1069 Lee, J. E., Pierrehumbert, R., Swann, A. and Lintner, B. R.: Sensitivity of stable water
1070 isotopic values to convective parameterization schemes, Geophys. Res. Lett., 36, doi:
1071 10.1029/2009gl040880, 2009.
1072 LeGrande, A. N. and Schmidt, G. A.: Sources of Holocene variability of oxygen isotopes in
1073 paleoclimate archives, Clim Past, 5(3), 441–455, 2009.
1074 Lehmann, M. and Siegenthaler, U.: Equilibrium oxygen- and hydrogen-isotope fractionation
1075 between ice and water, J. Glaciol., 37(125), 23–26, 1991.
1076 Lewis, S. C., LeGrande, A. N., Kelley, M. and Schmidt, G. A.: Water vapour source impacts
1077 on oxygen isotope variability in tropical precipitation during Heinrich events, Clim Past,
1078 6(3), 325–343, doi: 10.5194/Cp-6-325-2010, 2010.
1079 Lewis, S. C., LeGrande, A. N., Kelley, M. and Schmidt, G. A.: Modeling insights into
1080 deuterium excess as an indicator of water vapor source conditions, J. Geophys. Res.
1081 Atmos., 118(2), 243–262, doi: 10.1029/2012JD017804, 2013.
1082 Lohmann, G.: Atmospheric and oceanic freshwater transport during weak Atlantic
1083 overturning circulation, Tellus Series a-Dynamic Meteorology and Oceanography, 55(5),
1084 438–449, 2003.
1085 Lorius, C., Merlivat, L., Jouzel, J. and Pourchet, M.: 30,000-Year isotope climatic record
1086 from Antarctic ice, Nature, 280(5724), 644–648, 1979.
1087 Macdonald, R. W., Paton, D. W., Carmack, E. C. and Omstedt, A.: The fresh-water budget
1088 and under-ice spreading of Mackenzie River water in the Canadian Beaufort Sea based on
1089 salinity and O-18/O-16 measurements in water and ice, J. Geophys. Res., 100(C1), 895–
1090 919, doi: 10.1029/94JC02700, 1995.
1091 Maher, B. A. and Thompson, R.: Oxygen isotopes from Chinese caves: records not of
1092 monsoon rainfall but of circulation regime, J. Quat. Sci., 27(6), 615–624,

1093 doi:10.1002/jqs.2553, 2012.
1094 Majoube, M.: Fractionnement en oxygènè 18 et en deutérium entre l'eau et sa vapeur, Journal
1095 de Chimie et Physique, 68, 1423–1436, 1971.
1096 MARGO Project Members: Constraints on the magnitude and patterns of ocean cooling at the
1097 Last Glacial Maximum, Nature Geoscience, 2(2), 127–132, doi: 10.1038/Ngeo411, 2009.
1098 Marsland, S. J., Haak, H., Jungclaus, J. H., Latif, M. and Roske, F.: The Max-Planck-Institute
1099 global ocean/sea ice model with orthogonal curvilinear coordinates, Ocean Modelling,
1100 5(2), 91–127, 2003.
1101 Masson-Delmotte, V., Jouzel, J., Landais, A., Stiévenard, M., Johnsen, S. J., White, J. W. C.,
1102 Werner, M., Sveinbjornsdottir, A. and Fuhrer, K.: GRIP deuterium excess reveals rapid
1103 and orbital-scale changes in Greenland moisture origin, Science, 309(5731), 118–121,
1104 2005.
1105 Masson-Delmotte, V., Kageyama, M., Braconnot, P., Charbit, S., Krinner, G., Ritz, C.,
1106 Guilyardi, E., Jouzel, J., Abe-Ouchi, A., Crucifix, M., Gladstone, R. M., Hewitt, C. D.,
1107 Kitoh, A., LeGrande, A. N., Marti, O., Merkel, U., Motoi, T., Ohgaito, R., Otto-Bliesner,
1108 B., Peltier, W. R., Ross, I., Valdes, P. J., Vettoretti, G., Weber, S. L., Wolk, F. and Yu, Y.:
1109 Past and future polar amplification of climate change: climate model intercomparisons and
1110 ice-core constraints, Clim. Dyn., 26(5), 513–529, doi: 10.1007/S00382-005-0081-9, 2006.
1111 Merlivat, L. and Jouzel, J.: Global climatic interpretation of the deuterium-oxygen 18
1112 relationship for precipitation, J. Geophys. Res., 84(C8), 5029–5033, 1979.
1113 Meyer, H., Opel, T., Laepple, T., Dereviagin, A. Y., Hoffmann, K. and Werner, M.: Long-
1114 term winter warming trend in the Siberian Arctic during the mid- to late Holocene, Nature
1115 Geoscience, 8(2), 122–125, doi: 10.1038/ngeo2349, 2015.
1116 NEEM community members: Eemian interglacial reconstructed from a Greenland folded ice
1117 core, Nature, 493(7433), 489–494, doi: 10.1038/nature11789, 2013.
1118 North Greenland Ice Core Project members: High-resolution record of Northern Hemisphere
1119 climate extending into the last interglacial period, Nature, 431(7005), 147–151, doi:
1120 10.1038/Nature02805, 2004.
1121 Paul, A., Mulitza, S. and Pätzold, J.: Simulation of oxygen isotopes in a global ocean model,
1122 in: Use of proxies in paleoceanography: examples from the South Atlantic, edited by G.
1123 Fisher and G. Wefer, pp. 655–686, Springer, Berlin, Heidelberg. 1999.
1124 Pfahl, S. and Sodemann, H.: What controls deuterium excess in global precipitation? Clim
1125 Past, 10(2), 771–781, doi: 10.5194/cp-10-771-2014, 2014.
1126 Raddatz, T. J., Reick, C. H., Knorr, W., Kattge, J., Roeckner, E., Schnur, R., Schnitzler, K.
1127 G., Wetzel, P. and Jungclaus, J.: Will the tropical land biosphere dominate the climate-
1128 carbon cycle feedback during the twenty-first century? Clim. Dyn., 29(6), 565–574, doi:
1129 10.1007/S00382-007-0247-8, 2007.
1130 Risi, C., Bony, S., Vimeux, F. and Jouzel, J.: Water-stable isotopes in the LMDZ4 general
1131 circulation model: Model evaluation for present-day and past climates and applications to
1132 climatic interpretations of tropical isotopic records, J. Geophys. Res. Atmos., 115(D12),
1133 doi: 10.1029/2009JD013255, 2010a.
1134 Risi, C., Bony, S., Vimeux, F., Frankenberg, C., Noone, D. and Worden, J.: Understanding
1135 the Sahelian water budget through the isotopic composition of water vapor and
1136 precipitation, J. Geophys. Res., 115(D24), doi: 10.1029/2010JD014690, 2010b.
1137 Risi, C., Landais, A., Winkler, R. and Vimeux, F.: Can we determine what controls the spatio-
1138 temporal distribution of d-excess and O-17-excess in precipitation using the LMDZ

general circulation model? Clim Past, 9(5), 2173–2193, doi:10.5194/cp-9-2173-2013, 2013.

Roche, D. M. and Caley, T.: delta O-18 water isotope in the iLOVECLIM model (version 1.0) - Part 2: Evaluation of model results against observed delta O-18 in water samples, Geosci. Model Dev., 6(5), 1493–1504, doi: 10.5194/gmd-6-1493-2013, 2013.

Roche, D., Paillard, D., Ganopolski, A. and Hoffmann, G.: Oceanic oxygen-18 at the present day and LGM: equilibrium simulations with a coupled climate model of intermediate complexity, Earth Planet. Sci. Lett., 218(3-4), 317–330, doi: 10.1016/S0012-821x(03)00700-3, 2004.

Roche, D. M., Paillard, D., Caley, T. and Waelbroeck, C.: LGM hosing approach to Heinrich Event 1: results and perspectives from data–model integration using water isotopes, Quaternary Sci Rev, 106, 247–261, doi: 10.1016/j.quascirev.2014.07.020, 2014.

Roeckner, E., Baeuml, G., Bonaventura, L., Brokopf, R., Esch, M., Giorgetta, M., Hagemann, S., Kirchner, I., Kornblueh, L., Manzini, E., Rhodin, A., Schlese, U., Schulzweida, U. and Tompkins, A.: The general circulation model ECHAM5. Part I: Model description, Max Planck Institute for Meteorology, Hamburg. 2003.

Roeckner, E., Brokopf, R., Esch, M., Giorgetta, M., Hagemann, S., Kornblueh, L., Manzini, E., Schlese, U. and Schulzweida, U.: Sensitivity of simulated climate to horizontal and vertical resolution in the ECHAM5 atmosphere model, J. Climate, 19(16), 3771–3791, 2006.

Rozanski, K., Araguasaraguas, L. and Gonfiantini, R.: Relation between long-term trends of O-18 isotope composition of precipitation and climate, Science, 258(5084), 981–985, 1992.

Schäfer-Neth, C. and Paul, A.: Gridded global LGM SST and salinity reconstruction, doi: 10.1029/2006GL029067/full, 2003a.

Schäfer-Neth, C. and Paul, A.: The Atlantic Ocean at the Last Glacial Maximum: 1. Objective mapping of the GLAMAP sea-surface conditions, in: The South Atlantic in the late Quaternary - material budget and current systems, edited by G. Wefer, S. Mulitza, and V. Ratmeyer, pp. 531–548, Springer, Berlin, Heidelberg. 2003b.

Schmidt, G. A.: Oxygen-18 variations in a global ocean model, Geophys. Res. Lett., 25(8), 1201–1204, 1998.

Schmidt, G. A.: Forward modeling of carbonate proxy data from planktonic foraminifera using oxygen isotope tracers in a global ocean model, Paleoceanography, 14(4), 482–497, 1999.

Schmidt, G. A., Bigg, G. R. and Rohling, E. J.: Global seawater oxygen-18 database, available from: http://www.giss.nasa.gov/data/o18data, 1999.

Schmidt, G. A., LeGrande, A. N. and Hoffmann, G.: Water isotope expressions of intrinsic and forced variability in a coupled ocean-atmosphere model, J. Geophys. Res., 112(D10), doi: 10.1029/2006jd007781, 2007.

Schrag, D. P., Adkins, J. F., McIntyre, K., Alexander, J. L., Hodell, D. A., Charles, C. D. and McManus, J. F.: The oxygen isotopic composition of seawater during the Last Glacial Maximum, Quaternary Sci Rev, 21(1-3), 331–342, doi:10.1016/S0277-3791(01)00110-X, 2002.

Shackleton, N. J.: Attainment of isotopic equilibrium between ocean water and the benthonic foraminifera genus Uvigerina: isotopic changes in the ocean during the last glacial, Vol. 219. 1974.

Shah, A. M., Morrill, C., Gille, E. P., Gross, W. S., Anderson, D. M., Bauer, B. A., Buckner, R. and Hartman, M.: Global speleothem oxygen isotope measurements since the Last Glacial Maximum, Dataset Papers in Science, 2013, doi: 10.7167/2013/548048, 2013.

Sharp, Z.: Principles of Stable Isotope Geochemistry, Pearson Prentice Hall, Upper Saddle River, New Jersey, 2007.

Steen-Larsen, H. C., Johnsen, S. J., Masson-Delmotte, V., Stenni, B., Risi, C., Sodemann, H., Balslev-Clausen, D., Blunier, T., Dahl-Jensen, D., Ellehøj, M. D., Falourd, S., Grindsted, A., Gkinis, V., Jouzel, J., Popp, T., Sheldon, S., Simonsen, S. B., Sjolte, J., Steffensen, J. P., Sperlich, P., Sveinbjornsdottir, A. E., Vinther, B. M. and White, J. W. C.: Continuous monitoring of summer surface water vapor isotopic composition above the Greenland ice sheet, Atmos. Chem. Phys., 13(9), 4815–4828, doi: 10.5194/acp-13-4815-2013, 2013.

Steen-Larsen, H. C., Masson-Delmotte, V., Hirabayashi, M., Winkler, R., Satow, K., Prié, F., Bayou, N., Brun, E., Cuffey, K. M., Dahl-Jensen, D., Dumont, M., Guillevic, M., Kipfstuhl, S., Landais, A., Popp, T., Risi, C., Steffen, K., Stenni, B. and Sveinbjornsdottir, A. E.: What controls the isotopic composition of Greenland surface snow? Clim Past, 10(1), 377–392, doi: 10.5194/cp-10-377-2014, 2014a.

Steen-Larsen, H. C., Sveinbjornsdottir, A. E., Peters, A. J., Masson-Delmotte, V., Guishard, M. P., Hsiao, G., Jouzel, J., Noone, D., Warren, J. K. and White, J. W. C.: Climatic controls on water vapor deuterium excess in the marine boundary layer of the North Atlantic based on 500 days of in situ, continuous measurements, Atmos. Chem. Phys., 14(15), 7741–7756, doi: 10.5194/acp-14-7741-2014, 2014b.

Steen-Larsen, H. C., Sveinbjornsdottir, A. E., Jonsson, T., Ritter, F., Bonne, J. L., Masson-Delmotte, V., Sodemann, H., Blunier, T., Dahl-Jensen, D. and Vinther, B. M.: Moisture sources and synoptic to seasonal variability of North Atlantic water vapor isotopic composition, J. Geophys. Res. Atmos., doi: 10.1002/2015JD023234, 2015.

Stenni, B., Masson-Delmotte, V., Johnsen, S., Jouzel, J., Longinelli, A., Monnin, E., Rothlisberger, R. and Selmo, E.: An oceanic cold reversal during the last deglaciation, Science, 293(5537), 2074–2077, 2001.

Stenni, B., Masson-Delmotte, V., Selmo, E., Oerter, H., Meyer, H., Roethlisberger, R., Jouzel, J., Cattani, O., Falourd, S., Fischer, H., Hoffmann, G., Iacumin, P., Johnsen, S. J., Minster, B. and Udisti, R.: The deuterium excess records of EPICA Dome C and Dronning Maud Land ice cores (East Antarctica), Quaternary Sci Rev, 29(1-2), 146–159, doi: 10.1016/J.Quascirev.2009.10.009, 2010.

Stepanek, C. and Lohmann, G.: Modelling mid-Pliocene climate with COSMOS, Geosci. Model Dev., 5(5), 1221–1243, doi: 10.5194/gmd-5-1221-2012, 2012.

Tan, M.: Circulation effect: response of precipitation delta O-18 to the ENSO cycle in monsoon regions of China, Clim. Dyn., 42(3-4), 1067–1077, doi:10.1007/s00382-013-1732-x, 2014.

Thompson, L. G., Davis, M. E., Mosley-Thompson, E., Sowers, T. A., Henderson, K. A., Zagorodnov, V. S., Lin, P. N., Mikhalenko, V. N., Campen, R. K., Bolzan, J. F., Cole-Dai, J. and Francou, B.: A 25,000-year tropical climate history from Bolivian ice cores, Science, 282(5395), 1858–1864, 1998.

Thompson, L. G., Mosley-Thompson, E., Davis, M. E., Bolzan, J. F., Dai, J., Yao, T., Gundestrup, N. S., Wu, X., Klein, L. and Xie, Z.: Holocene-Late Pleistocene climatic ice core records from Qinghai-Tibetan Plateau, Science, 246, 474–477, 1989.

Thompson, L. G., Mosley-Thompson, E., Davis, M. E., Lin, P. N., Henderson, K. A., Coledai, J., Bolzan, J. F. and Liu, K. B.: Late glacial stage and Holocene tropical ice core records

From Huascaran, Peru, Science, 269(5220), 46–50, 1995.

Thompson, L. G., Mosley-Thompson, E., Davis, M. E., Henderson, K. A., Brecher, H. H., Zagorodnov, V. S., Mashiotta, T. A., Lin, P. N., Mikhalenko, V. N., Hardy, D. R. and Beer, J.: Kilimanjaro ice core records: Evidence of Holocene climate change in tropical Africa, Science, 298(5593), 589–593, 2002.

Tian, L., Yao, T., Schuster, P. F., White, J. W. C., Ichiyanagi, K., Pendall, E., Pu, J. and Wu, Y.: Oxygen-18 concentrations in recent precipitation and ice cores on the Tibetan Plateau, J. Geophys. Res. Atmos., 108(D9), 4293, doi: 10.1029–2002JD002173, 2003.

Tindall, J. C., Valdes, P. J. and Sime, L. C.: Stable water isotopes in HadCM3: Isotopic signature of El Nino Southern Oscillation and the tropical amount effect, J. Geophys. Res., 114, doi: 10.1029/2008jd010825, 2009.

Uemura, R., Masson-Delmotte, V., Jouzel, J., Landais, A., Motoyama, H. and Stenni, B.: Ranges of moisture-source temperature estimated from Antarctic ice cores stable isotope records over glacial–interglacial cycles, Clim Past, 8(3), 1109–1125, doi: 10.5194/cp-8-1109-2012, 2012.

Valcke, S., Caubel, A., Declat, D. and Terray, L.: OASIS3 Users's Guide, CERFACS, Toulouse, France. 2003.

Vimeux, F., Masson, V., Jouzel, J., Stiévenard, M. and Petit, J. R.: Glacial-interglacial changes in ocean surface conditions in the southern hemisphere, Nature, 398(6726), 410–413, 1999.

Vimeux, F., Gallaire, R., Bony, S., Hoffmann, G. and Chiang, J.: What are the climate controls on δD in precipitation in the Zongo Valley (Bolivia)? Implications for the Illimani ice core interpretation, Earth Planet. Sci. Lett., 240(2), 205–220, doi:10.1016/j.epsl.2005.09.031, 2005.

Wackerbarth, A., Scholz, D., Fohlmeister, J. and Mangini, A.: Modelling the delta O-18 value of cave drip water and speleothem calcite, Earth Planet. Sci. Lett., 299, 387–397, doi: 10.1016/j.epsl.2010.09.019, 2010.

WAIS Divide Project Members: Onset of deglacial warming in West Antarctica driven by local orbital forcing, Nature, doi: 10.1038/nature12376, 2013.

Wang, Y. J., Cheng, H., Edwards, R. L., An, Z. S., Wu, J. Y., Shen, C. C. and Dorale, J. A.: A High-Resolution Absolute-Dated Late Pleistocene Monsoon Record from Hulu Cave, China, Science, 294(5550), 2345–2348, doi: 10.1126/science.1064618, 2001.

Wang, Y., Cheng, H., Edwards, R. L., Kong, X., Shao, X., Chen, S., Wu, J., Jiang, X., Wang, X. and An, Z.: Millennial- and orbital-scale changes in the East Asian monsoon over the past 224,000 years, Nature, 451(7182), 1090–1093, doi: 10.1038/Nature06692, 2008.

Wei, W. and Lohmann, G.: Simulated Atlantic multidecadal oscillation during the Holocene, J. Climate, 25(20), 6989–7002, doi: 10.1175/JCLI-D-11-00667.1, 2012.

Wei, W., Lohmann, G. and Dima, M.: Distinct modes of internal variability in the global meridional overturning circulation associated with the Southern Hemisphere westerly winds, J. Phys. Oceanogr., 42(5), 785–801, doi: 10.1175/JPO-D-11-038.1, 2012.

Werner, M. and Heimann, M.: Modeling interannual variability of water isotopes in Greenland and Antarctica, J. Geophys. Res., 107(D1), 4001, doi: 10.1029/2001JD900253, 2002.

Werner, M., Mikolajewicz, U., Heimann, M. and Hoffmann, G.: Borehole versus isotope temperatures on Greenland: Seasonality does matter, Geophys. Res. Lett., 27(5), 723–726, 2000.

Werner, M., Heimann, M. and Hoffmann, G.: Isotopic composition and origin of polar precipitation in present and glacial climate simulations, Tellus Ser. B-Chem. Phys. Meteorol., 53(1), 53–71, 2001.

Werner, M., Langebroek, P. M. and Carlsen, T.: Stable water isotopes in the ECHAM5 general circulation model: Toward high‐resolution isotope modeling on a global scale, J. Geophys. Res. Atmos., doi: 10.1029/2011jd015681, 2011.

Xu, X.: Variations of oceanic and foraminiferal oxygen isotopes at the present day and the Last Glacial Maximum: Equilibrium simulations with an oceanic general circulation model, Universität Bremen, Alfred-Wegener-Institut, available from: http://hdl:10013/epic.40883, 2012.

Xu, X., Werner, M., Butzin, M. and Lohmann, G.: Water isotope variations in the global ocean model MPI-OM, Geosci. Model Dev., 5(3), 809–818, doi: 10.5194/gmd-5-809-2012, 2012.

Yao, T., Thompson, L., Yang, W., Yu, W., Gao, Y., Guo, X., Yang, X., Duan, K., Zhao, H., Xu, B., Pu, J., Lu, A., Xiang, Y., Kattel, D. B. and Joswiak, D.: Different glacier status with atmospheric circulations in Tibetan Plateau and surroundings, Nat Clim Change, 2(9), 663–667, doi: 10.1038/nclimate1580, 2012.

Zaucker, F. and Broecker, W. S.: The influence of atmospheric moisture transport on the fresh water balance of the Atlantic drainage basin: General circulation model simulations and observations, J. Geophys. Res., 97(D3), 2765–2773, doi: 10.1029/91JD01699, 1992.

Zhang, X., Lohmann, G., Knorr, G. and Xu, X.: Different ocean states and transient characteristics in Last Glacial Maximum simulations and implications for deglaciation, Clim Past, 9(5), 2319–2333, doi: 10.5194/cp-9-2319-2013, 2013.

Zhang, X., Lohmann, G., Knorr, G. and Purcell, C.: Abrupt glacial climate shifts controlled by ice sheet changes, Nature, 512(7514), 290–294, doi: 10.1038/nature13592, 2014.

Zhuang, K. and Giardino, J. R.: Ocean cooling pattern at the Last Glacial Maximum, Advances in Meteorology, 2012, doi: 10.1155/2012/213743, 2012.

1307 **Table 1:** Selected ice core records, reported PI and Δ(LGM-PI) values of $\delta^{18}O$ and deuterium
1308 excess (dex). No correction for glacial $\delta^{18}O$ enrichment has been applied to the listed ice core
1309 values. All values are given in permill on the SMOW scale.

1310

Site	Lon	Lat	$\delta^{18}O_{PI}$	dex_{PI}	$\Delta\delta^{18}O_{LGM-PI}$	Δdex_{LGM-PI}
Vostok[1,2]	106.87	-78.47	-57	15.5	-4	-3
Dome F[2,3]	39.70	-77.32	-55	14	-4	-2.5
Dome B[1]	94.92	-77.08	-55	13.5	-5	
EDC[1,4]	123.35	-75.10	-50.9	8.9	-5.4	-3.2
EDML[3,4]	0.07	-75.00	-44.9	4.5	-5	-2.9
Taylor Dome[1]	158.72	-77.80	-38.9	4.9	-3	
Talos[3]	159.18	-72.82	-37.5	3.9	-5	
Byrd[1]	-119.52	-80.02	-32.9	4.5	-8	
Siple Dome[3]	-148.82	-81.67	-26.9	2.9	-8	
WDC[3]	-112.14	-79.46	-34		-8	
GRIP[1]	-37.63	72.58	-35	9.5	-7	-3
NGRIP[1,5]	-42.32	75.10	-35.2		-8	
NEEM[6]	-51.06	77.45			-7.5	
Camp Century[1,7]	-61.13	77.17	-28		-12.9	
Dye3[8]	-43.81	65.18	-30		-5.5	
Renland[1,8]	-25.00	72.00	-26.5		-5	
Huascaran[1]	-77.61	-9.11			-6.3	-4
Sajama[1]	-68.97	-18.10			-5.4	
Illimani[1]	-67.77	-16.62			-6	-4
Guliya[1]	81.48	35.28			-5.4	
Dunde[1]	96.00	38.00			-2	

1311
1312 References:
1313 [1]reported in Risi et al. (2010), [2]Uemura et al. (2012), [3]WAIS Divide Project Members (2013),
1314 [4]Stenni et al. (2010), [5]North Greenland Ice Core Project members (2004), [6]NEEM community
1315 members (2013), [7]Johnsen et al. (1972), [8]Johnsen et al. (2001)
1316

Table 2: Selected speleothem sites, reported PI and LGM values of $\delta^{18}O_c$ in calcite, and the calculated LGM-PI $\Delta\delta^{18}O_{c,LGM-PI}$ change. All values have been taken from a compilation by Shah et al. (2013) and represent 1,000yrs-averaged $\delta^{18}O_c$ values for both the LGM (defined here as period 19,000 to 22,000yrs B.P.) and the most recent 1,000yrs B.P (used as an estimate for $\delta^{18}O_{c,PI}$). For Botuverá Cave, Gunung Buda National Park, and Sanbao Cave mean values of several reported speleothem records have been calculated. All $\delta^{18}O_c$ values refer to the PDB standard.

Cave Name	Lon	Lat	$\delta^{18}O_{c,PI}$ [‰]	$\Delta\delta^{18}O_{c,LGM-PI}$ [‰]
Botuverá	-49.16	-27.22	-3.2	-0.3
Cold Air	29.11	-24.02	-4.3	1.2
Gunung Buda	114.80	4.03	-9.3	1.7
Jerusalem West	35.15	31.78	-4.9	1.4
NWSI	172.00	-42.00	-3.2	0.3
Sanbao	110.43	31.67	-8.8	0.1
Sofular	31.93	41.42	-8.1	-4.5
Soreq	35.03	31.45	-5.4	2.2

Figure Captions

Fig. 1. (a) Global distribution of simulated and observed annual mean $\delta^{18}O_p$ values in precipitation. The background pattern shows the $\delta^{18}O_p$ distribution as simulated by the ECHAM5/MPI-OM model setup. Data from 70 GNIP stations (see text), from 21 ice core records (Table 1) and 8 speleothem records (Table 2) are plotted as coloured symbols. **(b)** Modelled versus observed annual mean $\delta^{18}O_p$ at the different GNIP, speleothem, and ice cores sites. The black line represents the 1:1 line indicating a perfect model fit. **(c)** Observed (black crosses) and modelled (filled red circles) spatial $\delta^{18}O_p$-T-relationship for annual mean values of T and $\delta^{18}O_p$ at 71 sites, where observed annual mean temperatures are below +20°C. The black (red) solid line represents a linear fit of the observed (modelled) data set.

Fig. 2. (a) Global distribution of simulated and observed annual mean $\delta^{18}O_{oce}$ values in ocean surface waters (mean over depth interval between surface and 10m). The background pattern shows the $\delta^{18}O_{oce}$ distribution as simulated by the ECHAM5/MPI-OM model setup. Data entries from the GISS database are plotted as coloured symbols. **(b)** Anomaly plot for the difference of the mean modelled versus observational values ($\Delta\delta^{18}O_{oce} = \delta^{18}O_{oce} - \delta^{18}O_{GISS}$) at the positions of the GISS data entries. For the calculation of $\Delta\delta^{18}O_{oce}$, the month of sampling has been considered (see text for details).

Fig. 3. Scatter plots of observed present-day $\delta^{18}O_{oce}$ values from the GISS database versus modelled $\delta^{18}O_{oce}$ values of the PI simulation for following basins: **(a)** Atlantic Ocean, **(b)** Pacific Ocean, **(c)** Indian Ocean, **(d)** Arctic Ocean. The black lines represent the 1:1 line indicating a perfect model fit.

Fig. 4. Meridional section of the simulated $\delta^{18}O_{oce}$ values in **(a)** the Atlantic (zonal mean over 60°W to 0°W), **(b)** the Pacific (zonal mean over 150°E to 110°W). Data entries from the GISS database for the same regions (Atlantic Ocean: n = 5811, Pacific Ocean: n = 2985) are plotted as coloured symbols in panel **(c)** and **(d)**.

Fig. 5. Global distribution of the simulated annual mean $\delta^{18}O_R$ signal in **(a)** large rivers, **(b)** surface water runoff from coastal grid points into the oceans, as simulated by the hydrological discharge model (HD model) within the ECHAM5/MPI-OM setup.

Fig. 6. Global distribution of simulated and observed annual mean deuterium excess (dex) values in **(a)** evaporation, **(b)** precipitation, **(d)** ocean surface waters. The background pattern shows the dex distribution as simulated by ECHAM5/MPI-OM. In (b), data from 70 GNIP stations, and 21 ice cores from Greenland and Antarctica are plotted as coloured symbols. In (d), 153 data entries from the GISS database are plotted as coloured symbols. Comparison of observed present-day dex values in **(c)** precipitation (red symbols), and **(e)** in ocean surface waters (blue symbols) versus the corresponding modelled dex values of the PI simulation. The black lines in (c) and (e) represent the 1:1 line indicating a perfect model fit.

Fig. 7. (a) Background pattern: Simulated global pattern of annual mean surface temperature (T_{2m}) changes between the LGM and PI climate. Pollen-based reconstructed temperature changes by Bartlein et al. (2011) are shown as coloured symbols. **(b)** Comparison of reconstructed temperature changes shown in (a) versus the simulated LGM-PI cooling at the sample locations. The black line represents the 1:1 line indicating a perfect model fit. **(c)** Simulated global pattern of annual mean precipitation changes between the LGM and PI climate. **(d)** Comparison of reconstructed precipitation changes shown in (b) versus the simulated LGM-PI change at the sample locations The black line represents the 1:1 line indicating a perfect model fit.

Fig. 8. (a) Background pattern: Simulated global pattern of annual mean $\delta^{18}O_p$ changes in precipitation between the LGM and PI climate. Reconstructed $\delta^{18}O_p$ in precipitation changes of ice cores (Table 1) and $\delta^{18}O_c$ in calcite of speleothems (Table 2) are shown as coloured symbols. **(b)** Comparison of reconstructed $\delta^{18}O$ changes shown in (a) versus the simulated LGM-PI $\delta^{18}O$ changes at the same locations. Reconstructed $\delta^{18}O_p$ anomalies stem from the following archives: Antarctica (dark blue), Greenland (light blue), and tropical ice cores (grey). For speleothems, reconstructed and simulated $\delta^{18}O_c$ changes are shown (green). The black line represents the 1:1 line indicating a perfect model fit. **(c)** Histogram of calculated temporal LGM-PI $\delta^{18}O_p$-T-gradients for all grid cells with (i) an annual mean PI temperature

1388 below +20°C, and (ii) a simulated LGM-PI cooling of at least -2°. The dashed line indicates
1389 the modelled PI spatial $\delta^{18}O_p$-T-gradient (0.58‰/°C).

1390

1391 **Fig. 9.** Comparison of annual mean LGM $\delta^{18}O_p$ anomalies measured in ice cores from
1392 Antarctica and Greenland (blue bars) versus the simulated ECHAM5/MPI-OM LGM-PI $\delta^{18}O_p$
1393 changes (red bars) at the ice core locations.

1394

1395 **Fig. 10. (a)** Simulated global pattern of annual mean $\delta^{18}O_{oce}$ changes in ocean surface waters
1396 (0-50m depth) between the LGM and PI climate. **(b)** Calculated global pattern of annual mean
1397 $\delta^{18}O_c$ changes in calcite in ocean surface waters between the LGM and PI climate. The $\delta^{18}O_c$
1398 values are derived from the simulated $\delta^{18}O_{oce}$ changes shown in a) and the modelled LGM-PI
1399 ocean temperature changes (see text for details). **(c)** Difference between simulated LGM-PI
1400 $\delta^{18}O_c$ changes and LGM-Late Holocene $\delta^{18}O_c$ anomalies of a compilation of 114 planktic
1401 foraminifera data entries compiled by Caley et al. (2014b).

1402

1403 **Fig. 11.** Background pattern: Meridional section of the simulated annual mean LGM-PI $\delta^{18}O_c$
1404 in calcite changes in **(a)** the Atlantic (zonal over 60°W to 0°W), **(b)** the Pacific (zonal mean
1405 over 150°E to 110°W). Geographically related data entries from a compilation of 115 LGM-
1406 Late Holocene $\delta^{18}O_c$ anomalies of benthic foraminifera data compiled by Caley et al. (2014b)
1407 are plotted as coloured symbols (Atlantic Ocean: n = 29; Pacific Ocean: n = 12) in each panel.

1408

1409 **Fig. 12.** Global distribution of simulated annual mean LGM-PI deuterium excess (dex)
1410 changes in **(a)** continental precipitation, **(b)** water vapour of the lowest atmospheric model
1411 layer above the ocean surface.

1412

1413 **Fig. 13.** Comparison of annual mean LGM dex anomalies measured in ice cores from
1414 Antarctica and Greenland (blue bars) versus simulated LGM-PI dex changes (ECHAM5/MPI-
1415 OM: red bars; ECHAM5-wiso: light grey bars) at the ice core locations

1416

Fig. 14. Relation between simulated LGM-PI deuterium excess (dex) changes of Southern Hemisphere water vapour of the lowest atmospheric model layer above the ocean surface versus simulated LGM-PI changes of **(a)** relative humidity above the Southern Hemisphere ocean surface (rh; red symbols); **(b)** Southern Hemisphere sea surface temperatures (SST, blue symbols).

Figure 1

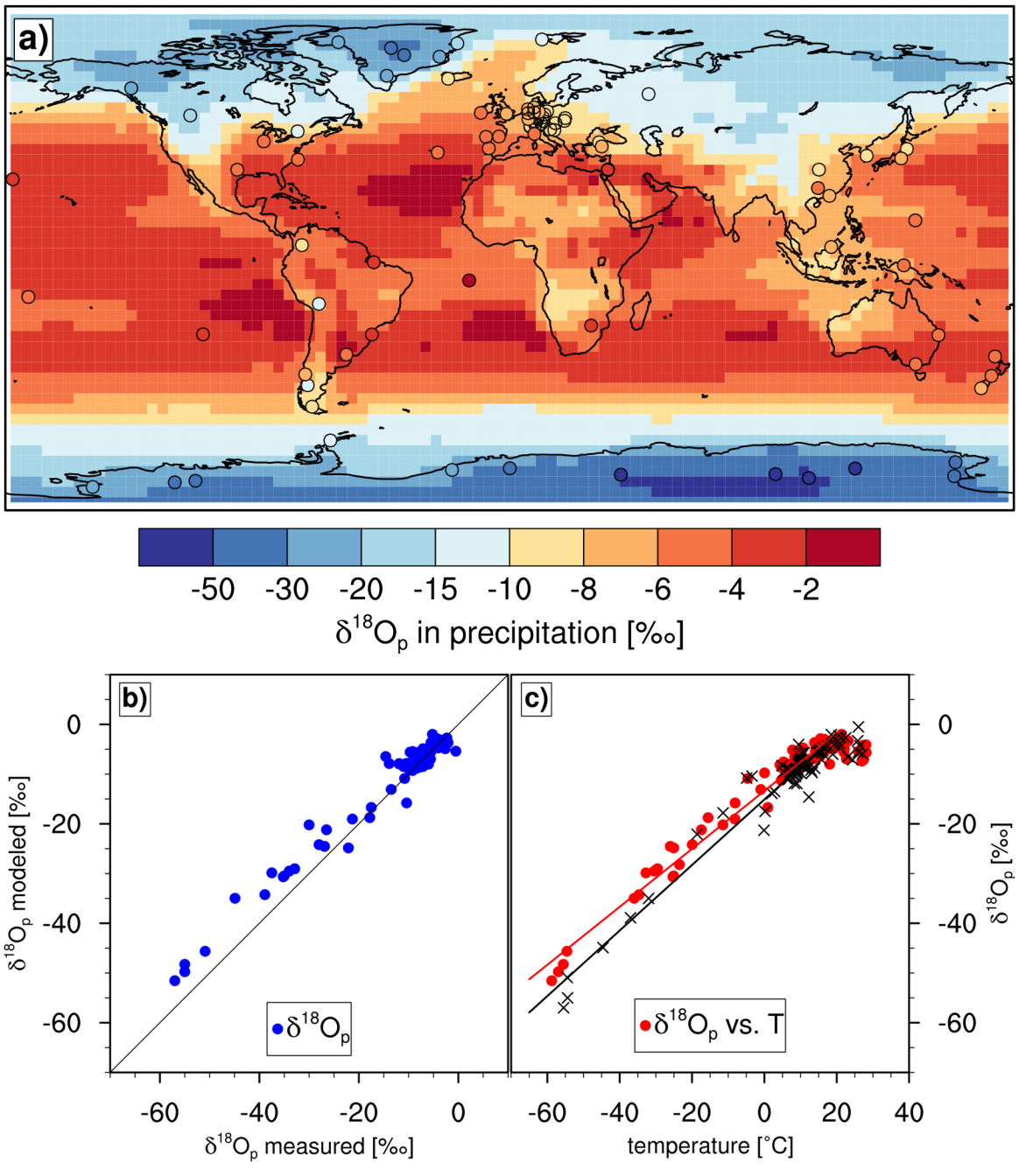
a)
-50 -30 -20 -15 -10 -8 -6 -4 -2
δ18Op in precipitation [‰]
b)
δ18Op
δ18Op modeled [‰]
δ18Op measured [‰]
c)
δ18Op vs. T
temperature [°C]
δ18Op [‰]

Figure 2

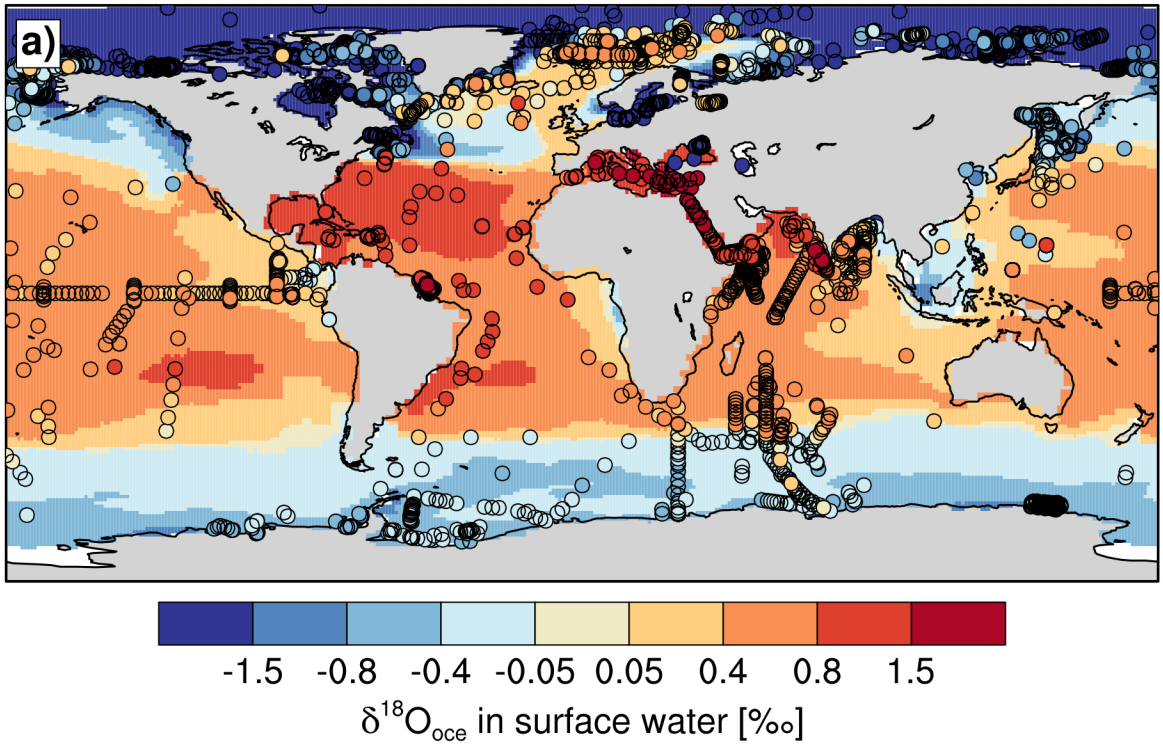
a)
-1.5 -0.8 -0.4 -0.05 0.05 0.4 0.8 1.5
δ18Ooce in surface water [‰]
b)
-2 -1 -0.5 -0.25 0.25 0.5 1 2
Δδ18Ooce in surface water [‰]

Figure 3

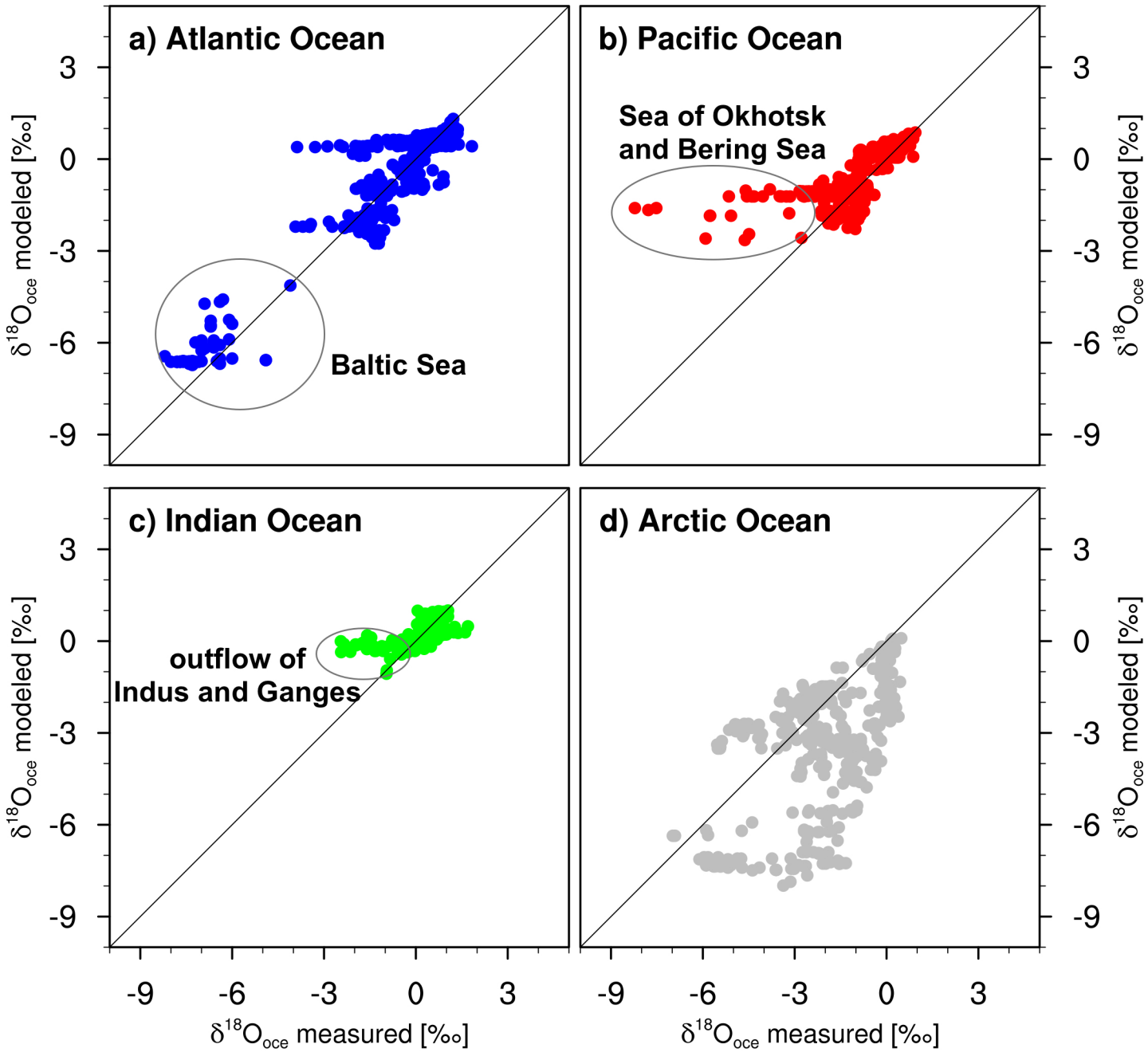
a) Atlantic Ocean
Baltic Sea
b) Pacific Ocean
Sea of Okhotsk
and Bering Sea
c) Indian Ocean
outflow of
Indus and Ganges
d) Arctic Ocean
δ18Ooce modeled [‰]
δ18Ooce measured [‰]
3
0
-3
-6
-9

Figure 4

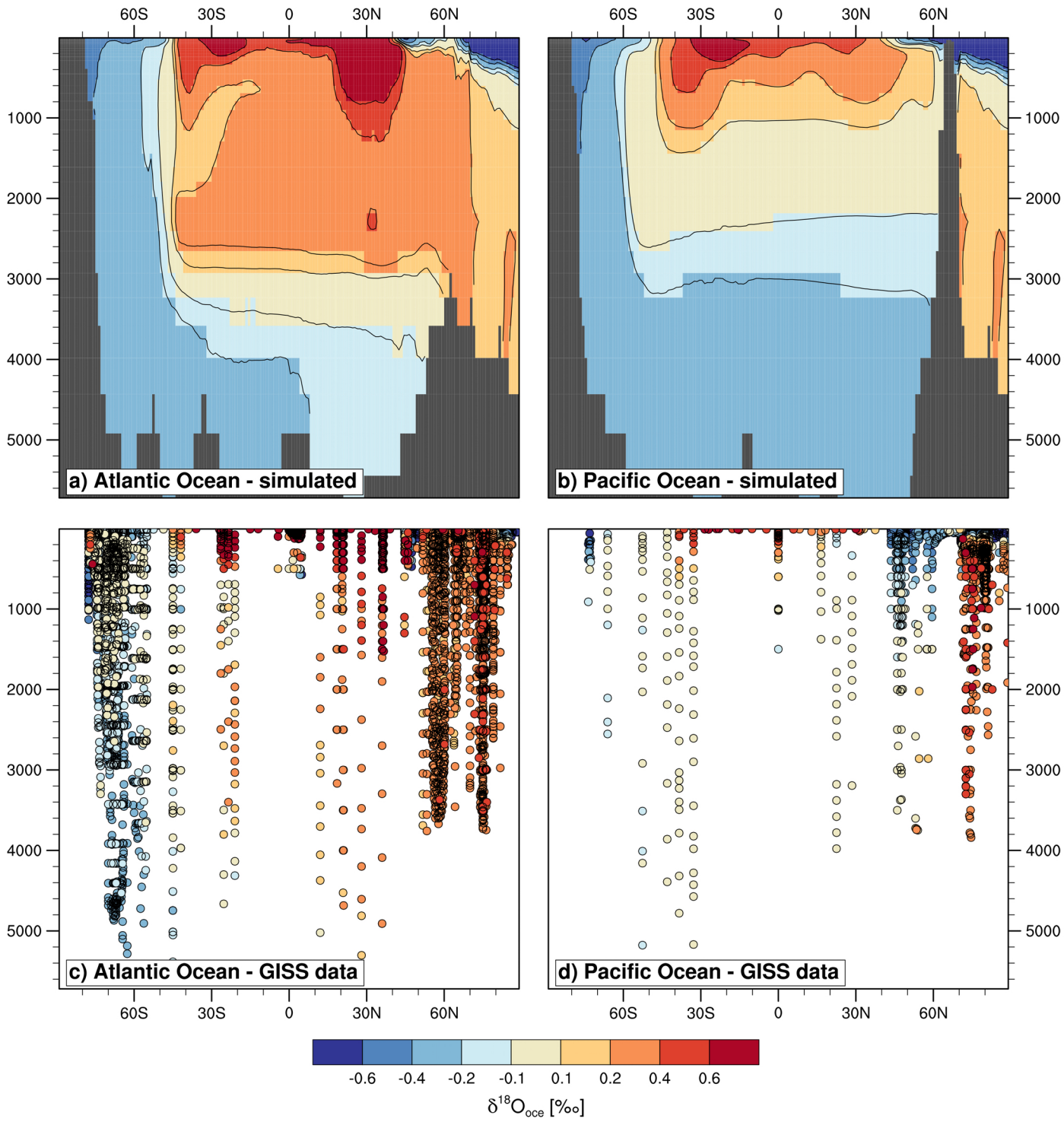
60S
30S
0
30N
60N
1000
2000
3000
4000
5000
a) Atlantic Ocean - simulated
b) Pacific Ocean - simulated
c) Atlantic Ocean - GISS data
d) Pacific Ocean - GISS data
-0.6
-0.4
-0.2
-0.1
0.1
0.2
0.4
0.6
δ18Ooce [‰]

Figure 5

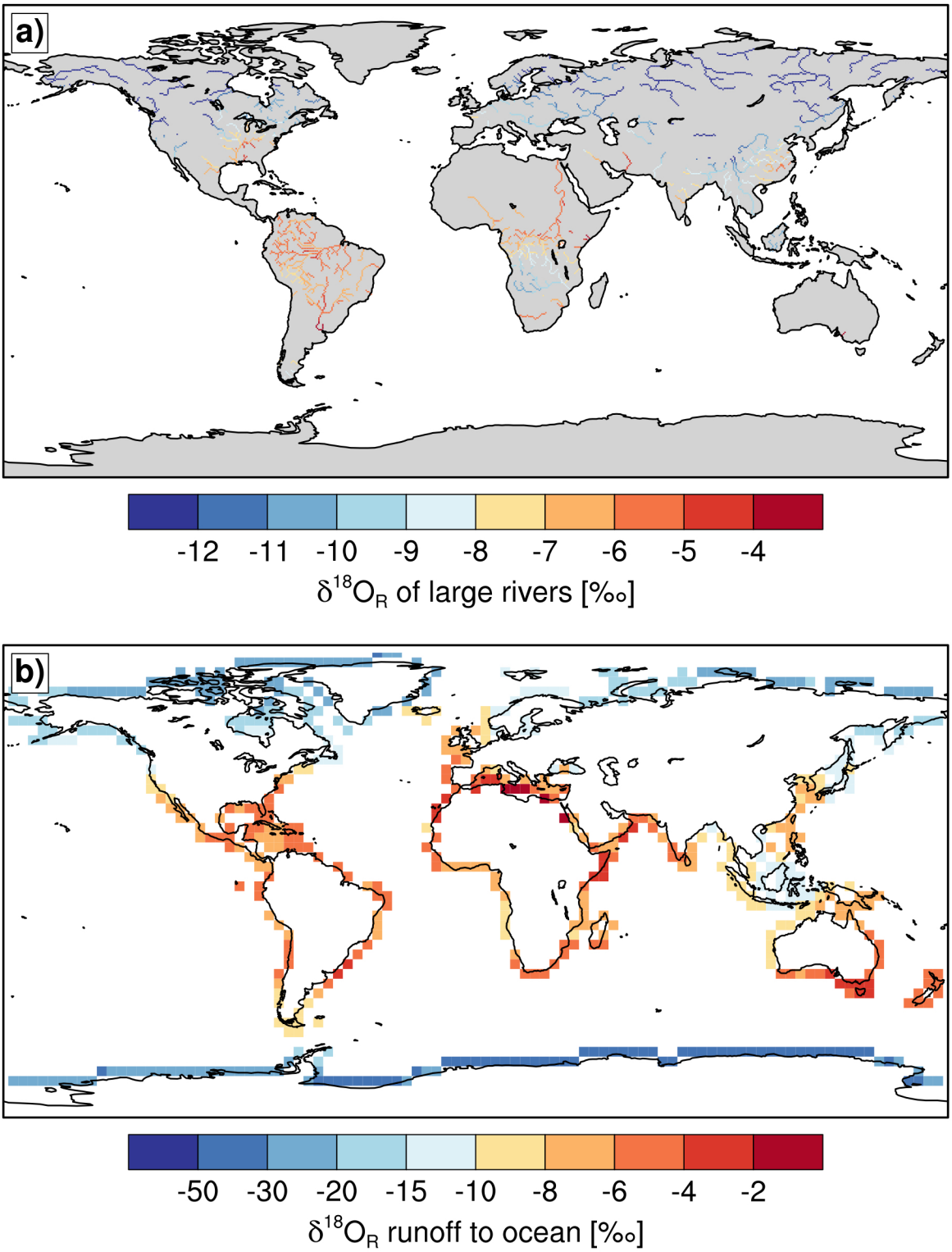
a)
-12 -11 -10 -9 -8 -7 -6 -5 -4
δ18OR of large rivers [‰]
b)
-50 -30 -20 -15 -10 -8 -6 -4 -2
δ18OR runoff to ocean [‰]

Figure 6

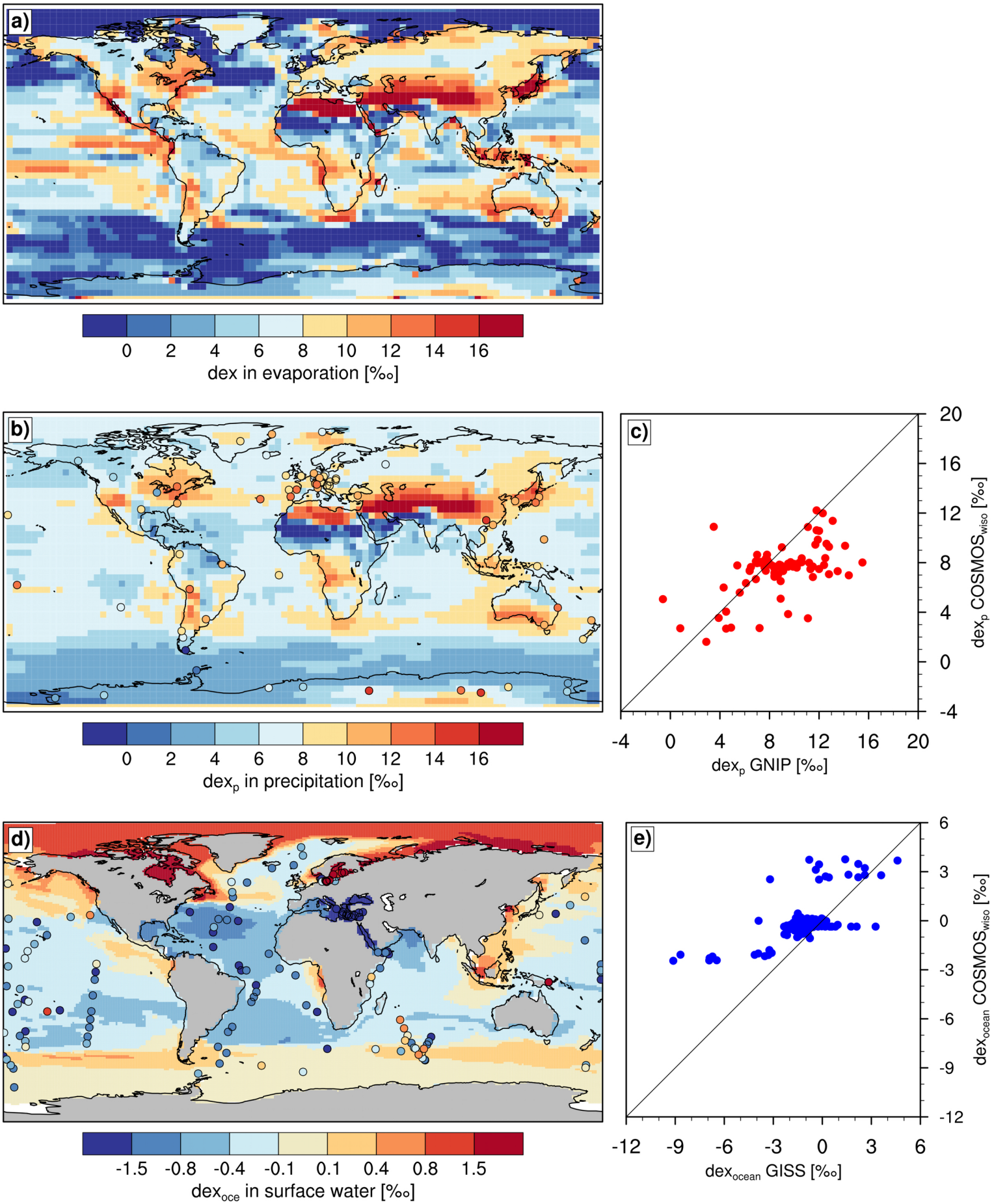
a)
0 2 4 6 8 10 12 14 16
dex in evaporation [‰]
b)
0 2 4 6 8 10 12 14 16
dex$_p$ in precipitation [‰]
c)
-4 0 4 8 12 16 20
dex$_p$ GNIP [‰]
20 16 12 8 4 0 -4
dex$_p$ COSMOS$_{wiso}$ [‰]
d)
-1.5 -0.8 -0.4 -0.1 0.1 0.4 0.8 1.5
dex$_{oce}$ in surface water [‰]
e)
-12 -9 -6 -3 0 3 6
dex$_{ocean}$ GISS [‰]
6 3 0 -3 -6 -9 -12
dex$_{ocean}$ COSMOS$_{wiso}$ [‰]

Figure 7

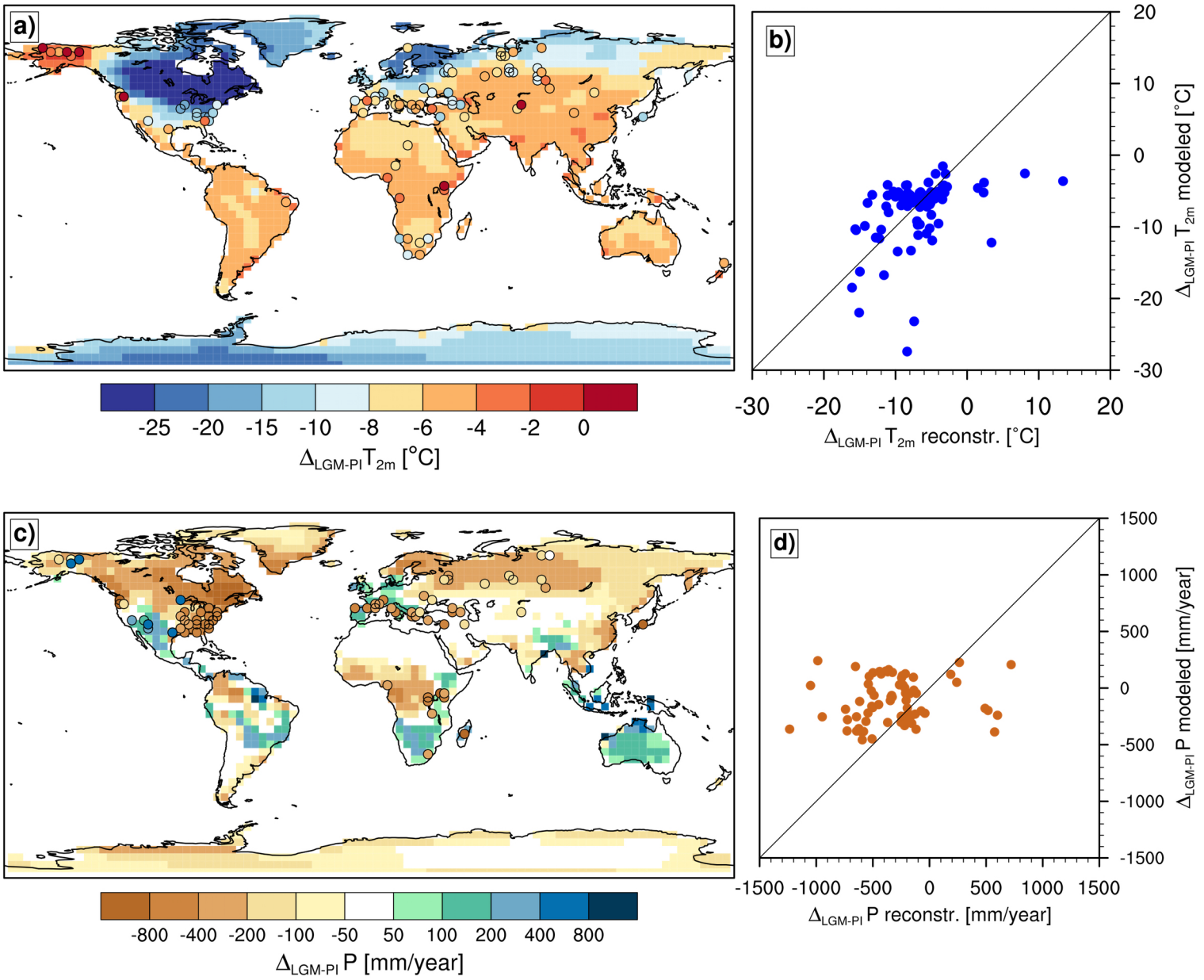
a)
-25 -20 -15 -10 -8 -6 -4 -2 0
ΔLGM-PI T2m [°C]
b)
20
10
0
-10
-20
-30
-30 -20 -10 0 10 20
ΔLGM-PI T2m reconstr. [°C]
ΔLGM-PI T2m modeled [°C]
c)
-800 -400 -200 -100 -50 50 100 200 400 800
ΔLGM-PI P [mm/year]
d)
1500
1000
500
0
-500
-1000
-1500
-1500 -1000 -500 0 500 1000 1500
ΔLGM-PI P reconstr. [mm/year]
ΔLGM-PI P modeled [mm/year]

Figure 8

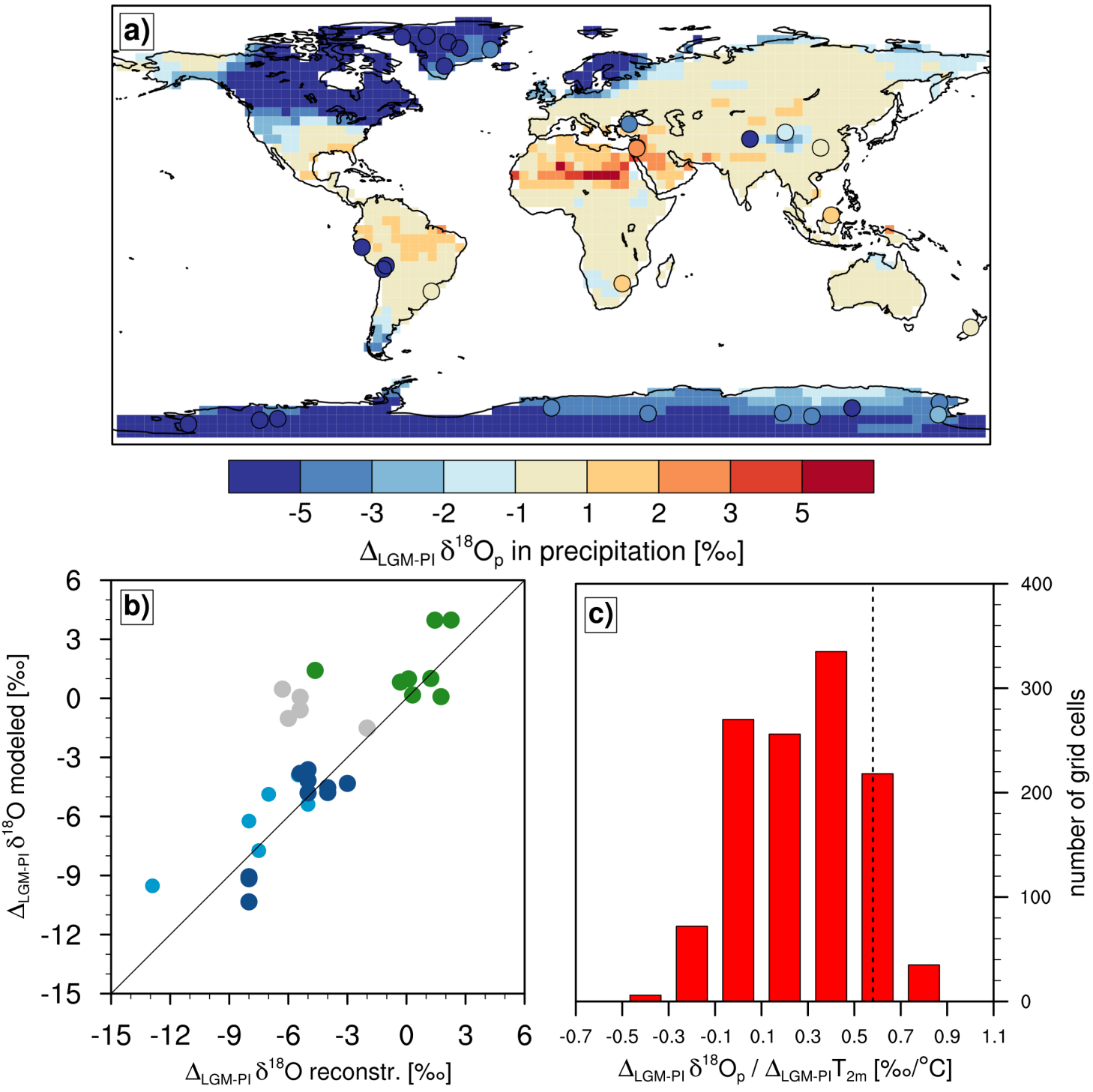
a)
-5
-3
-2
-1
1
2
3
5
$\Delta_{LGM-PI}\,\delta^{18}O_p$ in precipitation [‰]
b)
$\Delta_{LGM-PI}\,\delta^{18}O$ modeled [‰]
$\Delta_{LGM-PI}\,\delta^{18}O$ reconstr. [‰]
c)
number of grid cells
$\Delta_{LGM-PI}\,\delta^{18}O_p$ / $\Delta_{LGM-PI}T_{2m}$ [‰/°C]

Figure 9

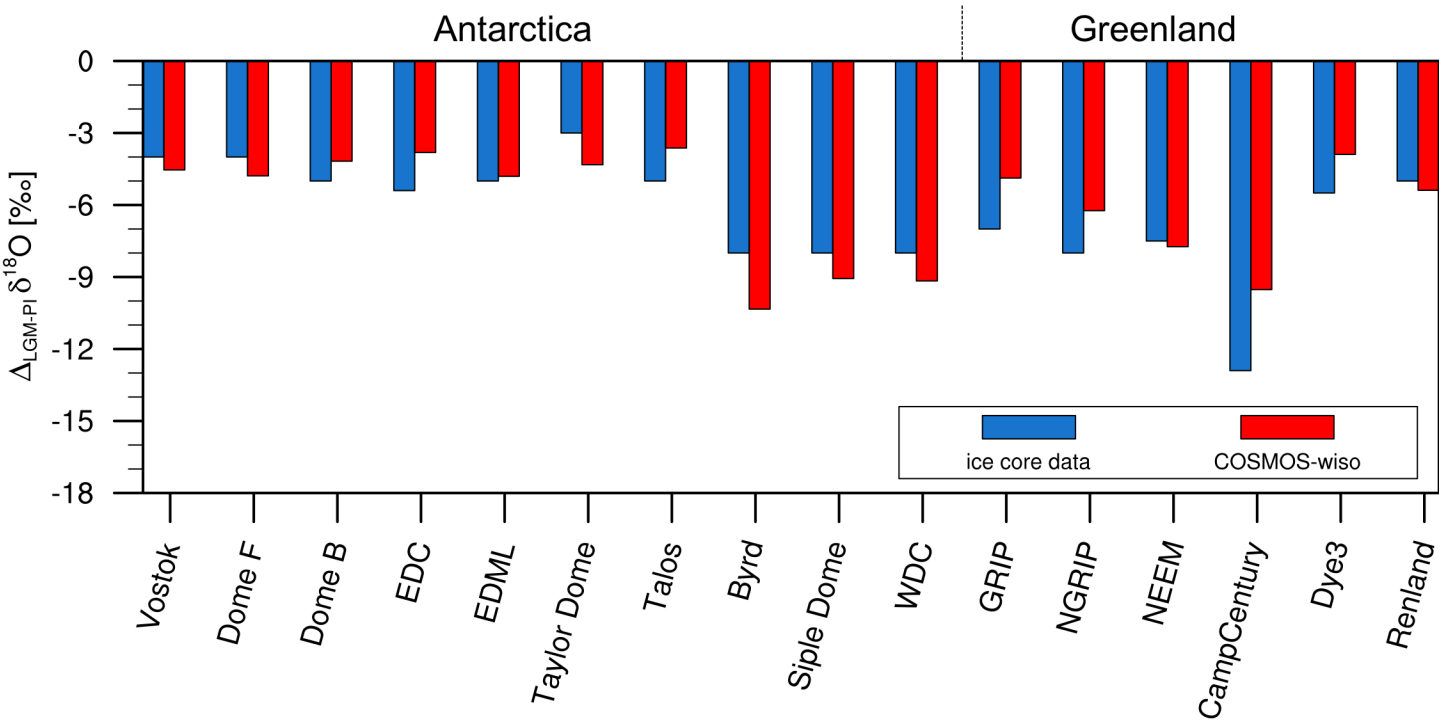
Antarctica
Greenland
0
-3
-6
-9
-12
-15
-18
$\Delta_{LGM-PI}\ \delta^{18}O$ [‰]
ice core data
COSMOS-wiso
Vostok
Dome F
Dome B
EDC
EDML
Taylor Dome
Talos
Byrd
Siple Dome
WDC
GRIP
NGRIP
NEEM
CampCentury
Dye3
Renland

Figure 10

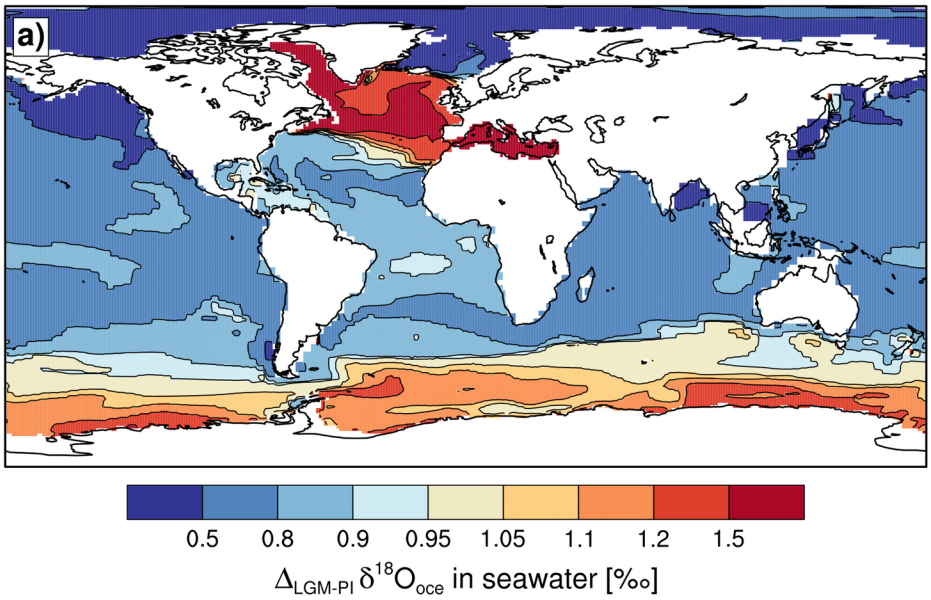
a)
0.5 0.8 0.9 0.95 1.05 1.1 1.2 1.5
$\Delta_{LGM-PI}\,\delta^{18}O_{oce}$ in seawater [‰]

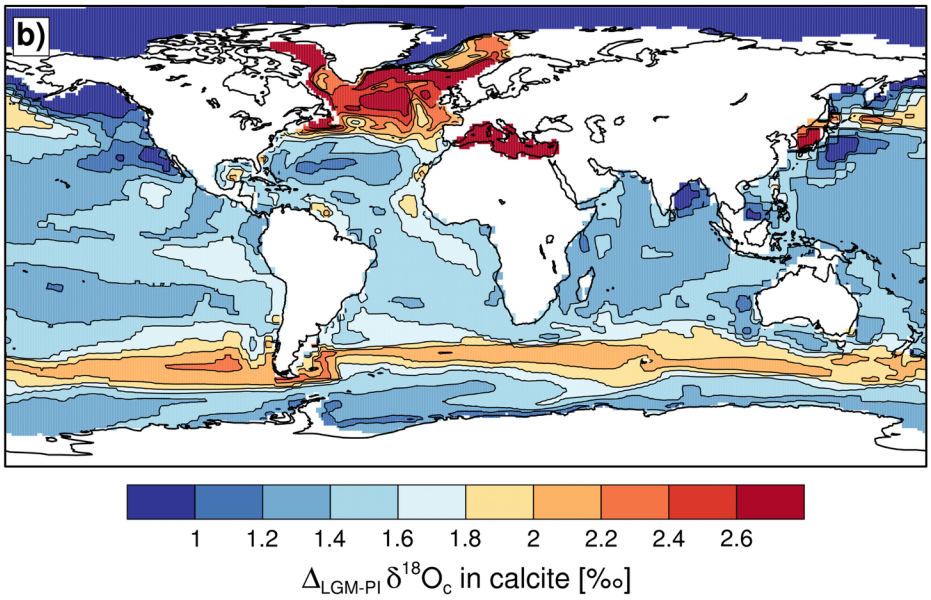
b)
1 1.2 1.4 1.6 1.8 2 2.2 2.4 2.6
$\Delta_{LGM-PI}\,\delta^{18}O_{c}$ in calcite [‰]

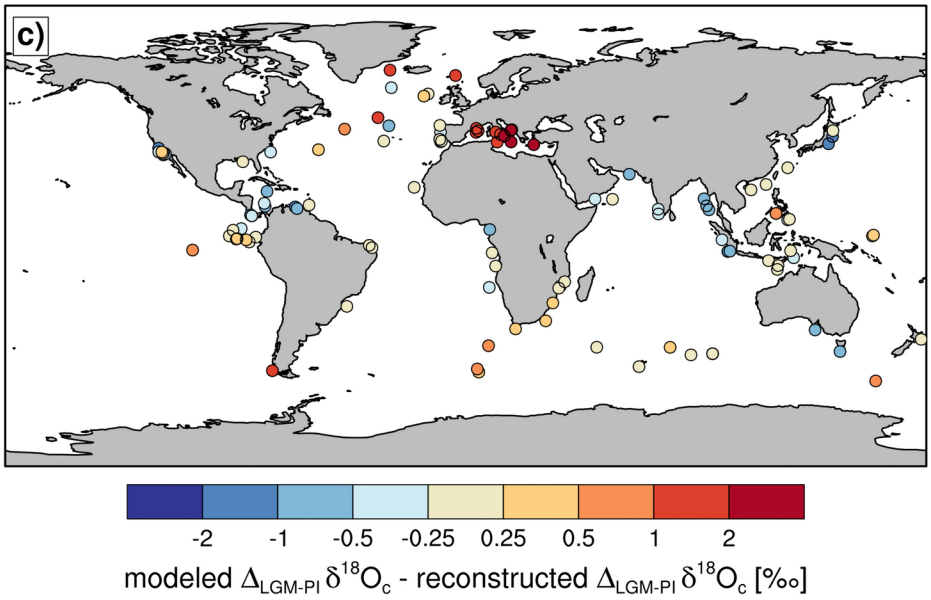
c)
-2 -1 -0.5 -0.25 0.25 0.5 1 2
modeled $\Delta_{LGM-PI}\,\delta^{18}O_{c}$ - reconstructed $\Delta_{LGM-PI}\,\delta^{18}O_{c}$ [‰]

Figure 11

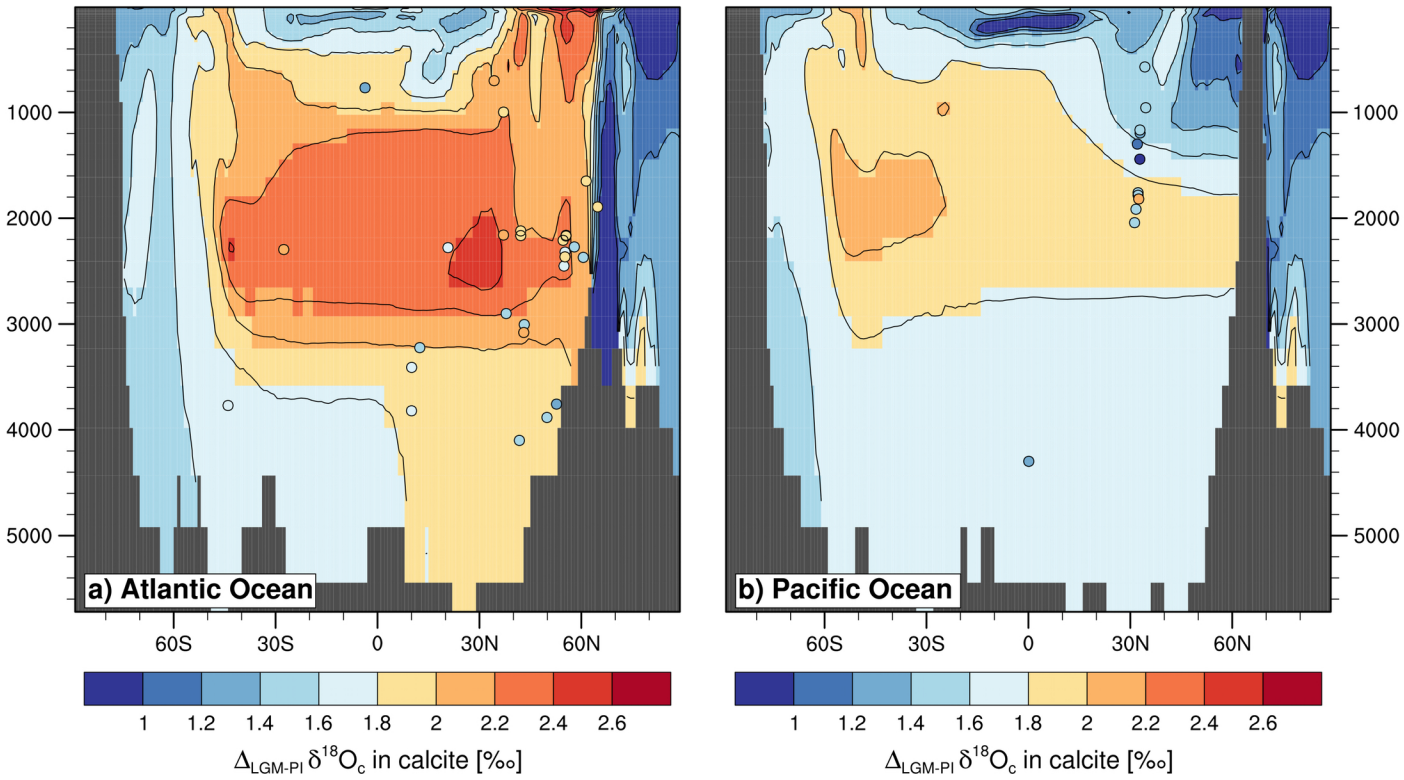
1000
2000
3000
4000
5000
a) Atlantic Ocean
60S
30S
0
30N
60N
1
1.2
1.4
1.6
1.8
2
2.2
2.4
2.6
$\Delta_{LGM-PI}\,\delta^{18}O_c$ in calcite [‰]
b) Pacific Ocean

Figure 12

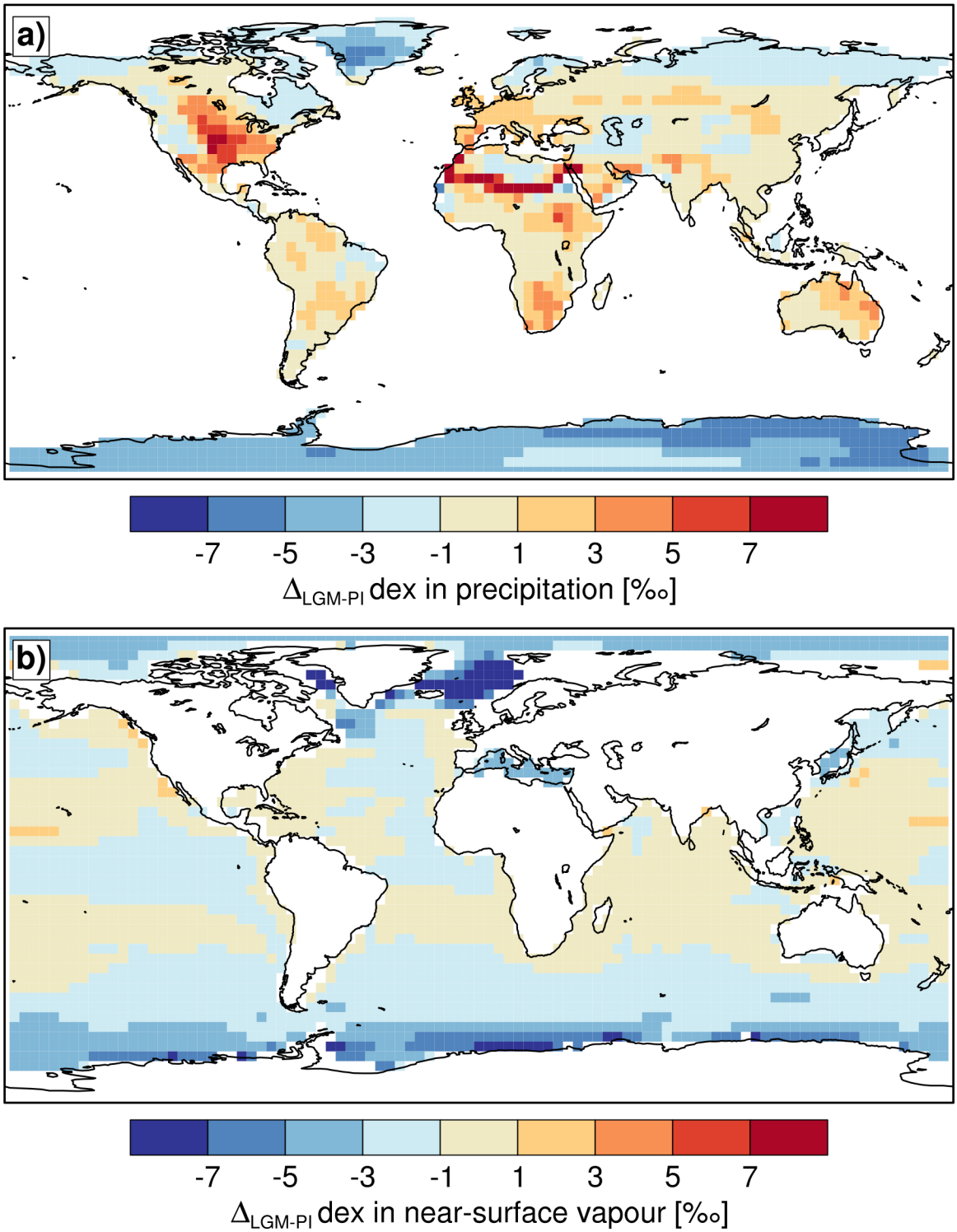
a)
-7
-5
-3
-1
1
3
5
7
Δ_{LGM-PI} dex in precipitation [‰]
b)
-7
-5
-3
-1
1
3
5
7
Δ_{LGM-PI} dex in near-surface vapour [‰]

Figure 13

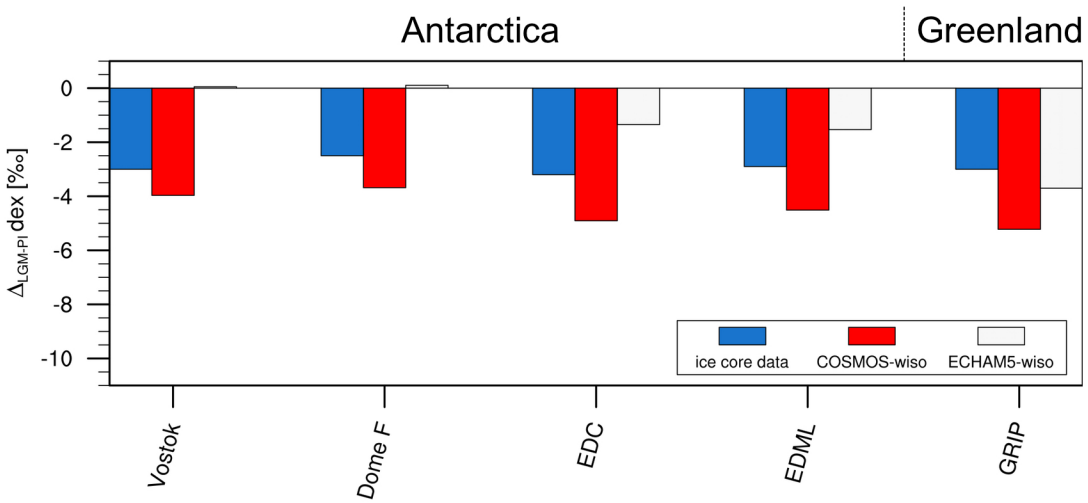
Antarctica
Greenland
0
-2
-4
-6
-8
-10
Δ_{LGM-PI} dex [‰]
ice core data
COSMOS-wiso
ECHAM5-wiso
Vostok
Dome F
EDC
EDML
GRIP

Figure 14

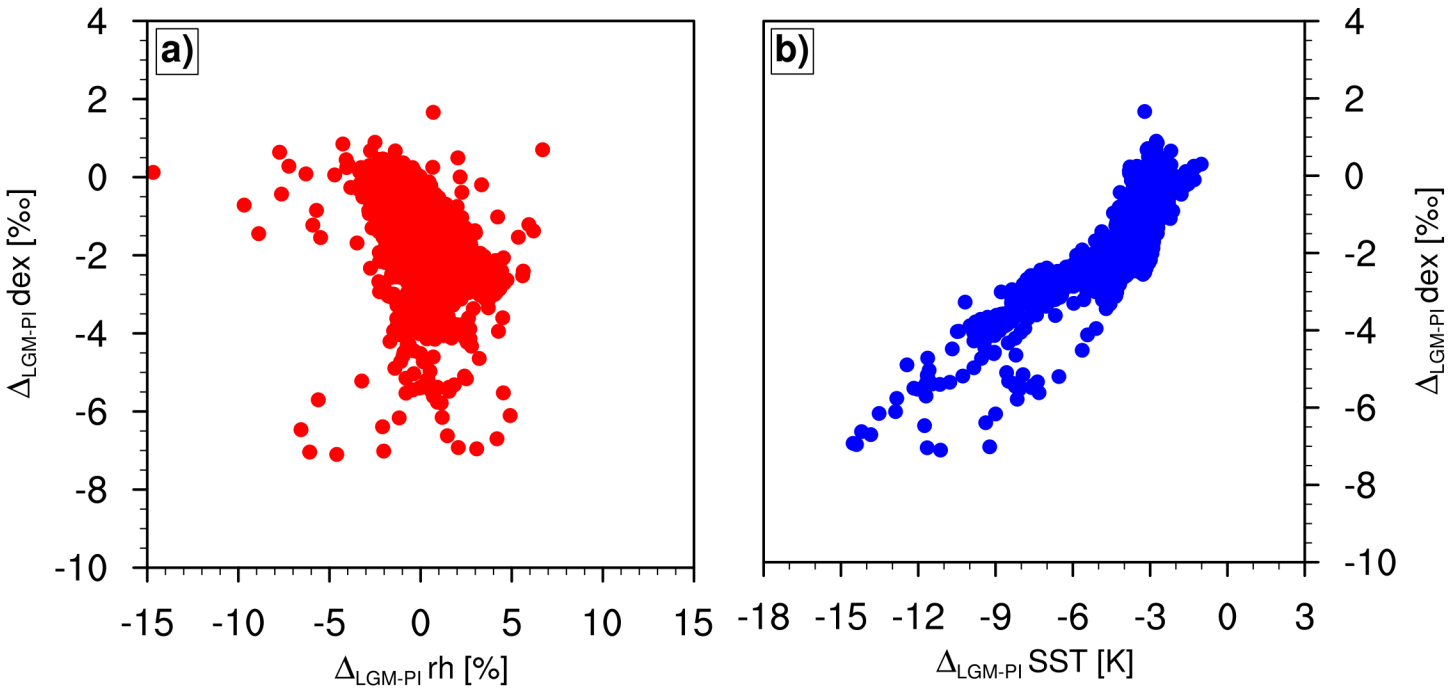
a)
b)
4
2
0
-2
-4
-6
-8
-10
-15
-10
-5
0
5
10
15
-18
-12
-9
-6
-3
3
Δ_{LGM-PI} dex [‰]
Δ_{LGM-PI} rh [%]
Δ_{LGM-PI} SST [K]